A TRIDENT SCHOLAR PROJECT REPORT

NO. 510

Near-Body Velocity and Turbulence Measurements in the Lee of an Inclined 6:1 Prolate Spheroid

by

Midshipman 1/C Zachary D. Nygaard, USN

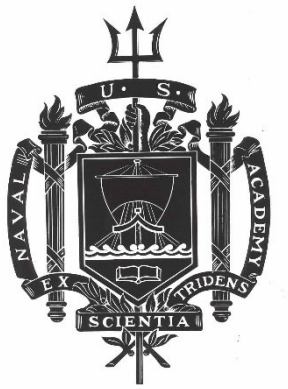

UNITED STATES NAVAL ACADEMY
ANNAPOLIS, MARYLAND

USNA-1531-2

REPORT DOCUMENTATION PAGE

Form Approved
OMB No. 0704-0188

1. REPORT DATE *(DD-MM-YYYY)*	**2. REPORT TYPE**	**3. DATES COVERED** *(From - To)*
7/12/21		

4. TITLE AND SUBTITLE
Near-Body Velocity and Turbulence Measurements in the Lee of an Inclined 6:1 Prolate Spheroid

5a. CONTRACT NUMBER

5b. GRANT NUMBER

5c. PROGRAM ELEMENT NUMBER

6. AUTHOR(S)
Nygaard, Zachary D.

5d. PROJECT NUMBER

5e. TASK NUMBER

5f. WORK UNIT NUMBER

7. PERFORMING ORGANIZATION NAME(S) AND ADDRESS(ES)

8. PERFORMING ORGANIZATION REPORT NUMBER

9. SPONSORING / MONITORING AGENCY NAME(S) AND ADDRESS(ES)
U.S. Naval Academy
Annapolis, MD 21402

10. SPONSOR/MONITOR'S ACRONYM(S)

11. SPONSOR/MONITOR'S REPORT NUMBER(S)
Trident Scholar Report no. 510 (2021)

12. DISTRIBUTION / AVAILABILITY STATEMENT

This document has been approved for public release; its distribution is UNLIMITED.

13. SUPPLEMENTARY NOTES

14. ABSTRACT

Despite dramatic advancements in computing power over the last several decades, computational fluid dynamics (CFD) models have not yet replaced experiments as the primary design and verification tool for the development of air- and water-borne vehicles. The benefits of advanced computational tools include the ability to iterate rapidly on a design, predict a wide range of parameters to include forces and moments, wake characteristics and acoustics, allow for design optimization, all relatively inexpensively. Experiments, on the other hand, are often expensive and time-consuming to conduct, and generally offer results over a narrow range of parameters. However, when conducted carefully at an appropriate model scale, the results provide a measure of certainty that is not yet offered by computational models. To improve CFD models, a more nuanced understanding is required of the flow physics that they describe. To that end, experiments are to be conducted in the large recirculating water channel at the U.S. Naval Academy. The flow in the near-body region of a 6:1 prolate spheroid measuring 0.43 m (17 in.) in length will be examined for length-based Reynolds numbers of 1 to 3×10^6 at angles of inclination of 2.5°, 5°, 10°, and 20°. Boundary layer trip designs will be evaluated and results compared to those of a smooth, un-tripped body. Velocity measurements will be made using a stereo particle image velocimetry (SPIV) system, with sufficient measurements taken to calculate mean flow and turbulence quantities. Results from this experiment will be made available for CFD verification and validation studies.

15. SUBJECT TERMS
Prolate spheroid, on-body, separation, mean flow, turbulence, boundary layer trip

16. SECURITY CLASSIFICATION OF:			**17. LIMITATION OF ABSTRACT**	**18. NUMBER OF PAGES**	**19a. NAME OF RESPONSIBLE PERSON**
a. REPORT	**b. ABSTRACT**	**c. THIS PAGE**		56	**19b. TELEPHONE NUMBER** *(include area code)*

U.S.N.A. --- Trident Scholar project report; no. 510 (2021)

NEAR-BODY VELOCITY AND TURBULENCE MEASUREMENTS IN THE LEE OF AN INCLINED 6:1 PROLATE SPHEROID

by

Midshipman 1/C Zachary D. Nygaard
United States Naval Academy
Annapolis, Maryland

Certification of Adviser Approval

LCDR Ethan E. Lust, USN
Mechanical Engineering Department

Acceptance for the Trident Scholar Committee

Professor Maria J. Schroeder
Associate Director of Midshipman Research

USNA-1531-2

Abstract:

Despite dramatic advancements in computing power over the last several decades, computational fluid dynamics (CFD) models have not yet replaced experiments as the primary design and verification tool for the development of air- and water-borne vehicles. The benefits of advanced computational tools include the ability to iterate rapidly on a design, predict a wide range of parameters to include forces and moments, wake characteristics and acoustics, allow for design optimization, all relatively inexpensively. Experiments, on the other hand, are often expensive and time-consuming to conduct, and generally offer results over a narrow range of parameters. However, when conducted carefully at an appropriate model scale, the results provide a measure of certainty that is not yet offered by computational models. To improve CFD models, a more nuanced understanding is required of the flow physics that they describe. This, ironically, requires more experimental data.

To that end, experiments are to be conducted in the large recirculating water channel at the U.S. Naval Academy. The flow in the near-body region of a 6:1 prolate spheroid measuring 0.43 m (17 in.) in length will be examined for length-based Reynolds numbers of 1 to 3×10^6 at angles of inclination of 2.5°, 5°, 10°, and 20°. Boundary layer trip designs will be evaluated and results compared to those of a smooth, un-tripped body. Velocity measurements will be made using a stereo particle image velocimetry (SPIV) system, with sufficient measurements taken to calculate mean flow and turbulence quantities. Results from this experiment will be made available for CFD verification and validation studies. They will also be used to inform follow-on experiments.

Key words: prolate spheroid, on-body, separation, mean flow, turbulence, boundary layer trip

Acknowledgments
I would like to thank my adviser, LCDR Ethan Lust, for his mentorship and steady guidance for the entirety of this research project, without which, this project could not have been completed. This research required a steep learning curve, with many difficulties along the way, but with the assistance and advisement of LCDR Lust, the overall experience of this project was incredibly beneficial. I would like to thank the entire Hydrolab team, Mr. Mike Stanbro, Mr. John Balano, Mr. Alex Laun, and Mr. Bill Beaver, for their help in planning for and developing our experimental apparatus. At innumerable points in this project, the Hydrolab team was instrumental in assisting with the many challenges faced throughout the duration of this research project. I would like to thank the machine shop, specifically Mr. Andrew Pullen, Mr. Brandon Stanley, Mr. Travis Ball, Mr. Ben Johnson, Mr. Mike Superczynski and Mr. Charlie Swanson, for their help in fabricating the spheroid, tunnel lid, and spheroid mounting system. As always, the machine shop's work was impeccable and timely. I would like to thank Dr. Peter Chang and ONR for their support in this research project.

Contents

Table of Figures

Nomenclature:

Semi-major axis	a
Semi-minor axis	b, c
Coefficient of force	C_F
Coefficient of moment	C_M
Spheroid diameter ($2b$)	D
Force	F
Spheroid length ($2a$)	L
Moment	M
Spheroid radius (b)	R
Diameter-based Reynolds number	Re_D
Length-based Reynolds number	Re_L
Surface-distance Reynolds number	Re_x
Streamwise coordinate along the body surface	s
Strouhal number	St
Streamwise velocity	U
Streamwise velocity	u
Vertical velocity	v
Horizontal velocity	w
Streamwise coordinate	x
Vertical coordinate	y
Horizontal coordinate	z
Area blockage ratio	β
Boundary layer thickness	δ
Vorticity	ζ
Angle of inclination	θ
Kinematic viscosity	ν
Density	ρ
Vortex shedding frequency	ω

1. Introduction

Despite years of effort and incredible growth in computing power, even the most capable of modern Computational Fluid Dynamics (CFD) codes cannot yet predict the velocity and pressure fields around a three-dimensional body with the desired accuracy at a reasonable computational cost. Without this ability, fundamental parameters such as forces (e.g. lift and drag) and moments exerted on the body by the fluid cannot be predicted. To improve CFD predictions, in terms of speed and accuracy, a more fundamental understanding of the underlying physics is needed. This fundamental understanding will likely come from experimental observations.

Of particular interest is the ability to predict, for a three-dimensional body 1) transition from laminar flow through transition to turbulent flow, 2) the pressure gradient along the body including the points of flow separation, and 3) the evolution of coherent turbulent structures in the wake of the body. Improved experimental observations in terms of increased measurement resolution, broadened spatial extent, and a wider range of experimental parameters – particularly high Reynolds number observations – are in great demand by the community of engineers and scientists developing CFD tools. The overall goal of this effort is to develop computational tools that can be used to design the next generation of aero- and hydrospace vehicles.

Over the last four decades, the 6:1 prolate spheroid, an ellipsoid of revolution, has emerged as a highly-desirable test case for verification and validation of CFD codes due to its simple geometric description but complex three-dimensional flow. As will be discussed in a following section, there is much experimental data with which to compare results, and much computational work from which to identify current needs.

The Office of Naval Research Advanced Naval Platforms Division (ONR 331) is responsible for advancing research in a variety of subject areas including basic research into hydrodynamics. This study is among the first of a number of related studies that is part of a multi-university effort culminating in very large scale testing at the Large Cavitation Channel (LCC) in Memphis planned for 2022-2023. The focus of the initiative is to improve our physical understanding of three-dimensional boundary layer development; transition, separation, and wake development on a canonical body that can also be used for verification and validation. The research group at the U.S. Naval Academy has been tasked with conducting preliminary testing of design parameters to inform full-scale model development. We will also serve as a test facility for the development and verification of novel flow measurement equipment.

1.1. **Theory**

A prolate spheroid (Figure 1) is an ellipsoid of revolution – a three-dimensional surface - specified by the following expression:

$$\frac{x^2}{a^2}+\frac{y^2}{b^2}+\frac{z^2}{c^2}=1 \tag{1}$$

Where x, y, and z are Cartesian coordinates, a is half of the major-axis length, b is half of the minor-axis length, which is equal to c for a spheroid which is axisymmetric. By definition, for a prolate spheroid, $a > b$ and c.

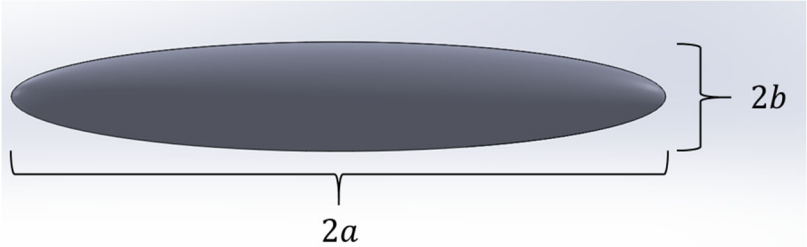

Figure 1: Prolate spheroid geometry. The major axis, a (defined as the length, L of the body) and the minor axis, b (defined as the diameter, D of the body). For an axisymmetric body, $b = c$.

The angle of inclination, α of the spheroid is the angle made between the major axis and the inflow, with 0° being parallel to the inflow. Positive angles of inclination generally describe a nose-down pitch, in keeping with the anti-clockwise positive convention used in Cartesian geometry.

The Reynolds number is a ratio of the inertial forces to the viscous forces in a flow. Its exact definition depends on the specific flow scenario, but for the purposes of this discussion, it is defined as:

$$Re_L = \frac{UL}{\nu} \tag{2}$$

where U is the magnitude of the inflow velocity, L is the length of the body ($2a$) in the direction of flow, and ν is the kinematic viscosity of the fluid. The power of the Reynolds number is that for any geometrically scaled body of any size immersed in any fluid – liquid or gas – if the Reynolds number is the same, the flow around the body and just downstream in the wake will look similar and have similar characteristics. This fact allows the comparison of flows at different scales; the representation of a full-sized ocean-going vessel (commonly referred to as the *prototype*) by a much smaller scale *model*, for example.

1.2. **Literature Review**

A number of experimental studies on 6:1 prolate spheroids have focused on on-body and near wake flow characteristics. Meier and Kreplin obtained data on the boundary layer and separation region from flow visualization, surface hot film, and pressure measurements [1]. Reynolds numbers from 7.2 to 9.6×10^6 were tested at angles of attack from 0° to 30°. It was determined that an increase in Reynolds number moves the location of separation forward on the body and increases the magnitude of the shear stress. Angles of attack at or above 10° produce wholly different flow fields, shown by the change in location of separation lines.

Barber and Simpson obtained boundary layer profiles and Reynolds shear stress measurements at two axial locations on the body of a 6:1 prolate spheroid for Reynolds numbers up to 4×10^6 and angles of inclination of 10° and 15° [2]. It was determined that near-body turbulence increased with Reynolds number and angle of inclination and that the boundary layer grows circumferentially and axially.

Ahn and Simpson investigated the dependence of boundary layer transition and separation phenomena on angle of attack and Reynolds number [3]. A critical Reynolds number of approximately 2.5×10^6 was identified as being the transition point along the body from laminar to transitional and turbulent separation. Results indicate that Reynolds number dependency of separation lines at Reynolds numbers above this critical value is greatly reduced.

Fu et al. documented the effects of boundary layer tripping, angle of attack, and Reynolds number on the flow structure in the lee side of a prolate spheroid [4]. It was also one of the first studies to use Particle Image Velocimetry (PIV) to observe the near-body flow field around a prolate spheroid. Results showed that the pair of vortex sheets produced on either lateral side of the body increased in vorticity with Reynolds number and inclination. Results also indicated that the majority of the circulation in the flow lies outside of the distinct vortical structure of the flow.

Goody, Simpson, and Engel employed the same model spheroid at the same angles of incidence at a Reynolds number of 4.2×10^6, measuring the velocity field with hot-wire velocimetry to further explore the near-body flow field [5]. At an inclination angle of 10° they showed that the turbulence was primarily located near the body, in contrast to observations at 20° in which the turbulence moved away from the body and into the wake region.

Chesnakas and Simpson used a three-dimensional LDV system to record velocity measurements with corresponding wall-pressure measurements from $y^+ = 7$ out beyond the boundary layer edge [6]. The generation of secondary streamlines were determined to be the clearest indicator of separation, reattachment, and vortical structures in the flow. Most relevant to the current study is the existence of a region just behind the separation lines and between the two separation sheets that is relatively quiescent. Most previous efforts were focused on near- or on-body flow behavior.

As of right now, there is no literature available which provides high resolution measurement of the velocity field while also capturing a large sweep of the velocity field. This research project helps fill the current gap by capturing this data in many different configurations due to the variations in Reynolds number, angle of inclination, trip, and the field of view captured.

2. Materials and Methods

2.1. **Test**

Tests were performed in the Large Re-Circulating Water Tunnel at the U.S. Naval Academy, a schematic of which is shown in Figure 2. The test section measures 0.41 m (16 in.) wide by 0.41 m (16 in.) tall by 1.5 m (60 in.) long. The maximum velocity in the test section is 7.62 m/s (25 ft/s).

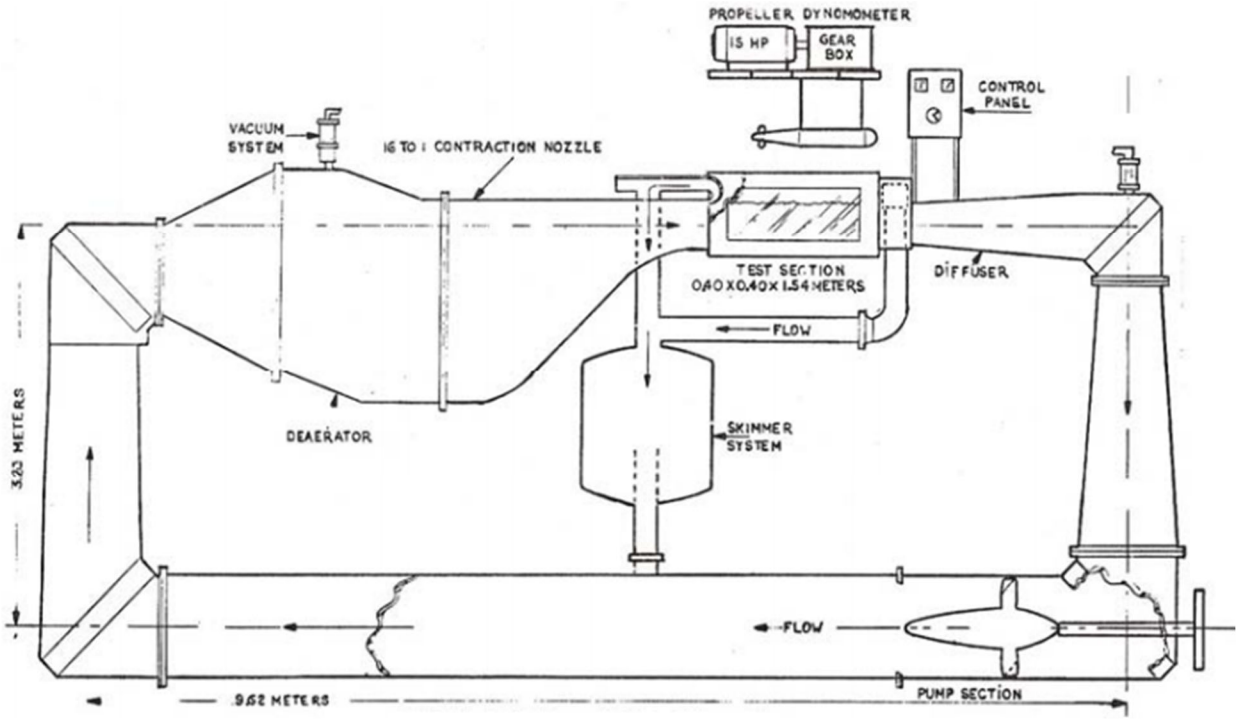

Figure 2: Schematic of the Large, Re-Circulating Water Tunnel [7].

2.2. **Spheroid Model and Sting Mount**

The prolate spheroid model (shown in Figure 3) has a 6:1 aspect ratio, with the length (tip to tail) of 0.432 m (17 in.) and minor axis length (diameter) of 0.072 m (2.84 in.). The length of the model was selected to maximize the length-based Reynolds number while keeping the blockage ratio ($\beta = A_{spheroid}/A_{tunnel}$) below 6%, a value recommended by [8] to preclude significant flow distortion. The model (shown in Figure 4) was made of 6061-T6 aluminum and anodized for corrosion resistance and to reduce laser light reflection. The spheroid also features a removable tip section from $x/L < 0.2$ that allows for different boundary layer trip geometries to be evaluated.

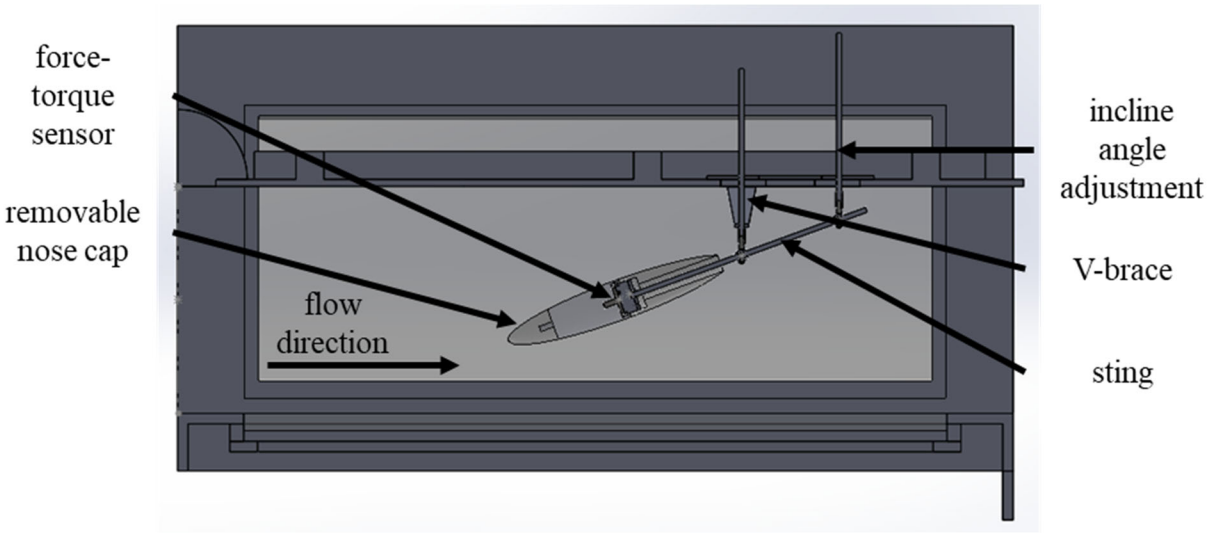

Figure 3: Schematic of spheroid and sting mount in the recirculating water tunnel.

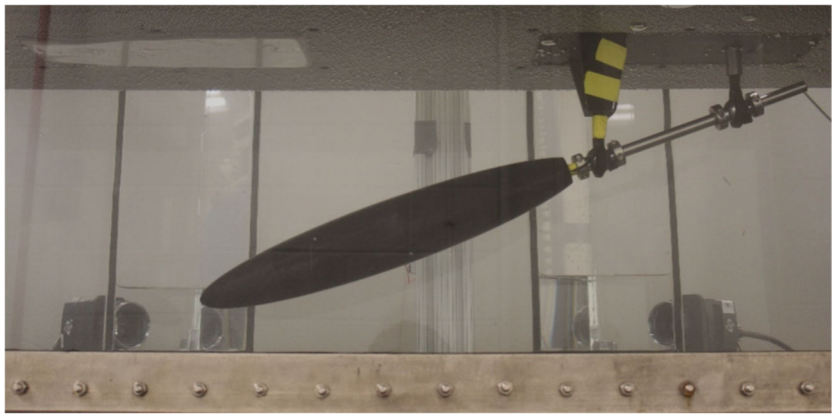

Figure 4: Model spheroid measuring 432 mm in length, shown at 20° inclination with flow from left to right.

The spheroid was sting-mounted on a 0.75 in. 316 stainless steel rod, suspended from the lid of the channel, as shown in Figure 3. The position and orientation of the spheroid was adjusted by changing the length of the vertical mount rods. The center of the spheroid was positioned in the geometric center of the tunnel, and was rotated about this point to change the angle of inclination. CAD model position and physical model position agree to within 0.25 in. From the CAD file shown in Figure 3, the spheroid and sting were manufactured in the USNA machine shop.

The static angle of the spheroid relative to the tunnel lid, was measured using a clear acrylic fixture and an inclinometer with a resolution of 0.1°, as shown in Figure 5.

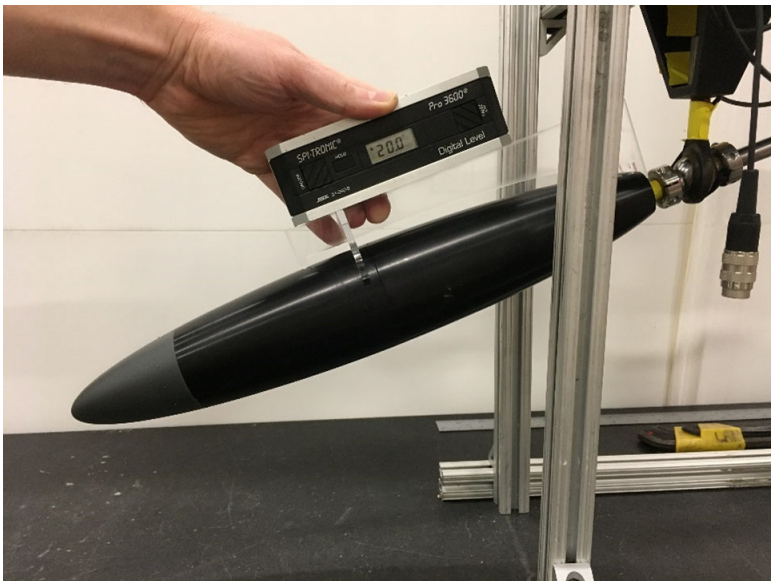

Figure 5: Verification of spheroid inclination angle. A clear acrylic fixture was created to allow for precise angle measurement of the body. An inclination angle of 20.0° is shown.

The absolute position of the spheroid was verified using a precision vertical height measuring instrument, as shown in Figure 6. The height of the tip of the body was found to be within 0.25 in of the height predicted by the CAD file.

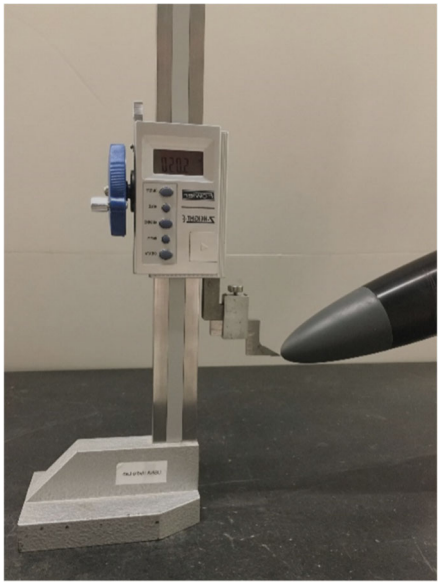

Figure 6: Spheroid tip height measurement.

2.3. **Boundary Layer Trip Design**

The boundary layer trip geometry used in the present study was proposed for planned experimental campaign to be conducted in the William B. Morgan Large Cavitation Channel (LCC). In addition to ensuring boundary layer transition from laminar to turbulent flow at the intended point, this geometry was intended to be simple enough to be easily modeled for CFD validation and verification.

The boundary layer trip geometry for the LCC test campaign was scaled for the present experiment and is defined as follows:

Location of trip pegs:	s_t = 142.6 mm (x/L = 0.17)
Spacing between pegs:	b = 14.8 mm
Number of pegs:	N = 12
Peg height:	h = 0.61 mm
Peg diameter:	d = 0.61 mm
Nose cone extent:	$0 \leq x \leq 86.4\ mm$ (x/L = 0.2)

A cartoon of the proposed trip design is shown in Figure 7.

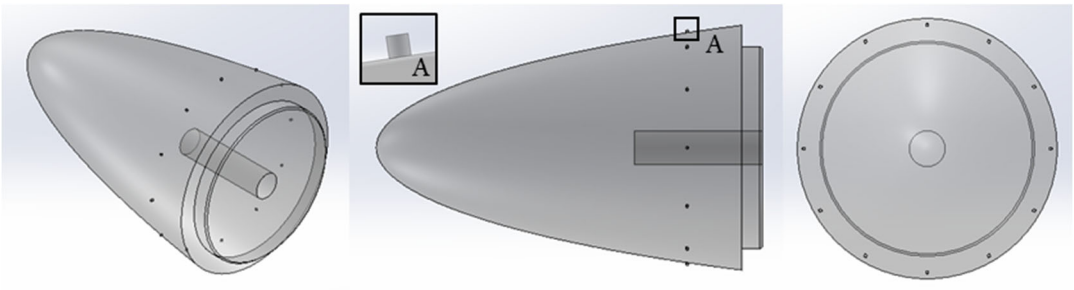

Figure 7: Proposed trip designs for the USNA model. The nose measures 86.4 mm long in the streamwise direction. Pegs are oriented normal to the surface, not the semi-major axis.

Trip scaling justification

The surface of the prolate spheroid is described by the following expression:

$$\frac{x^2}{a^2}+\frac{y^2}{b^2}+\frac{r^2}{c^2}=1 \tag{3}$$

Where a is the semi-major axis, b is the semi-minor axis, and for an axisymmetric body, $b = c$. For the USNA model, a is 216 mm and b is 36 mm. The length along the surface of the body, s is calculated using the following expression:

$$s=\frac{\pi}{2\sqrt{2}}\sqrt{(a-x)^2+(b-y)^2} \tag{4}$$

The lowest flow speed at which the surface length Reynolds number, Re_x reaches the critical value of 5×10^5 on the removable nose section ($x/L \leq 0.2$) of the USNA model corresponds to Re_L of 2.5×10^6 (5.79 m/s). Thus, this was taken to be the flow speed at which trip geometry is specified. At Re_L of 2.5×10^6, the trip location is at $x/L = 0.17$.

The height of pegs is determined using the Blasius boundary layer height equation. Given a kinematic viscosity of 1×10^{-6} m^2/s, the surface distance to the trip, s_t of 86 mm and a flow speed of 5.79 m/s, the boundary layer thickness at the trip, δ_t is approximately 0.61 mm.

The peg diameter was not directly specified for the LCC test. The only requirement is that it is sufficiently large to yield a diameter-based Reynolds number for the peg above 1,000 and thus the drag coefficient of the peg near unity. For the USNA model, the peg diameter was set to 0.61 mm (Re_d of 3,350) in order to strengthen the peg and to maintain the dimensional accuracy of the 3D printer used to make the nose. According to the printer documentation, dimensional accuracy can decrease with increasing aspect ratio for appendages.

The spacing between the trip pegs, b is specified by the following expression, developed in the *Considerations* document:

$$b=2\sqrt{\beta h d\left(C_D/C_f\right)\tan\theta} \tag{5}$$

Where β is a dimensionless coefficient, taken to be 5, which relates the skin friction force to the peg's drag disturbance, h is the height of the peg, d is the diameter of the peg, C_D/C_f is the ratio of the peg's drag coefficient to the skin-friction coefficient (assuming generic values of 1.0/0.003) and θ is the turbulent triangle spreading angle, taken to be 5°. For the USNA model, the resulting peg spacing is 14.8 mm.

At x = 73.44 mm, y = 27.04 mm and the circumference of the body is 169.9 mm. Dividing the circumference by the peg spacing indicates the number of pegs, N to be 11.5, or 12 pegs (also a factor of 360), spaced 30° apart. Pegs of these specifications are shown in Figure 7.

The nose was printed using FormLabs Tough 2000 resin and the finished product was machined to ensure a seamless fit with the spheroid body. The finished print was spray painted matte black to improve laser light absorption. The diameter of the printed pegs, including the spray paint, measured to within 0.07 mm of the 0.61 mm specified and the height of the pegs was within 0.02 mm of the value specified. The smooth nose and tripped geometry are shown in Figure 8.

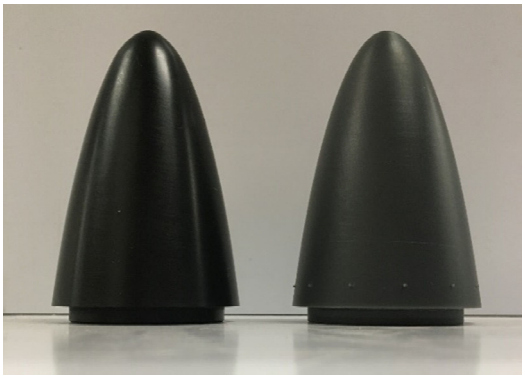

Figure 8: Smooth nose made of anodized aluminum (left) and nose featuring the boundary layer trip (design 1) made of FormLabs Tough 2000 resin (right). The nose with the trip was subsequently painted matte black to improve laser light absorption.

2.4. **Measurement of Digital Signals**

The inflow velocity was set using the tunnel flow speed control system and is independently measured using a floor-mounted pitot tube that is above the boundary layer. Additionally, the temperature of the water in the tunnel was recorded to allow calculation of the kinematic viscosity of the water, and thus the Reynolds number.

The axial force on the spheroid was measured using an ATI Industrial Automation Mini45 force-torque sensor, which was built to IP-68 waterproofing standards. By design, the measurement face of the sensor is located at the center of volume of the untruncated spheroid.

The appropriate sampling rate for the force-torque sensor is dictated primarily by the potential vibration frequency modes of the model. If the sampling frequency is smaller than the anticipated vibration frequency, the effects of any vibration will not be measured or observed. As significant vibrations could negatively impact measurements, it is necessary to be vigilant for their presence. The most likely cause of model vibration is vortex shedding. The frequency of the first mode of vortex shedding is predicted using the critical Strouhal number. The Strouhal number, St is a ratio of the speed of vibration to the mean flow speed:

$$St = \frac{L\omega}{U} \tag{6}$$

where ω is the shedding frequency. From previous observations [9], the critical Strouhal number was taken to be 0.8, which results in an anticipated vibration frequency of 12.8 Hz. In order to observe this frequency, the sampling rate must be set to at least twice this frequency, due to Nyquist sampling considerations. With a reasonable margin, the sampling frequency for the force-torque sensor was set to 50 Hz.

2.5. **Flow Field Measurement**

Flow field measurements were made with a stereo particle image velocimetry (SPIV) system, which provides three Cartesian velocity components (i.e. $\vec{V} = u, v, w$) in two spatial dimensions (3C2D). The system is comprised of two, TSI PowerView^{TM} 8 MP CCD cameras. The cameras feature a 3320 px by 2490 px CCD chip which measures 13.7 mm by 13.3 mm. With these cameras connected, the system is capable of capturing images at a rate of 3.75 Hz (every 0.267 s). At the time of sampling, each camera takes two images, separated in time by a user-specified Δt. Each sample includes four images and is referred to as a *realization*. Each image takes up 16 MB of memory, thus each realization requires 64 MB of memory.

Each camera is mounted to a translating breadboard, to which the laser and associated optics are also mounted. The entire SPIV system moves as a unit, sliding along linear rails mounted beneath the tunnel test section so that the light sheet and cameras remain in fixed positions relative to each other. Each camera was fitted with a 50 mm lens, which provided a nominal field of view of 170 mm wide by 100 mm in height (scaled as shown in Figure 4). With a 32 px by 32 px interrogation spot size and 50% overlap, the vector spacing was less than 0.7 mm between velocity measurements.

A laser was used to illuminate the particles in the flow. The laser used in the present experiment is a Quantel Evergreen Nd:YAG, dual-cavity 532 nm laser, capable of producing 200 mJ per pulse at a maximum repetition rate of 15 Hz per cavity. The laser firing and camera shutter control were coordinated in time by a digital synchronizer, which is connected to the PIV computer and controlled via TSI Insight^{TM} 4G software.

The beam produced by each laser cavity had a nominal diameter of 5 mm. Two cylindrical lenses with focal lengths of -20 mm and -25 mm, were used to form the beam into a light sheet of sufficient width to illuminate the entire field of view and a thickness of approximately 1.5 mm. Figure 8 displays the two planes in which the laser was oriented in the tunnel, laterally (Figure 8a) and longitudinally (Figure 8b).

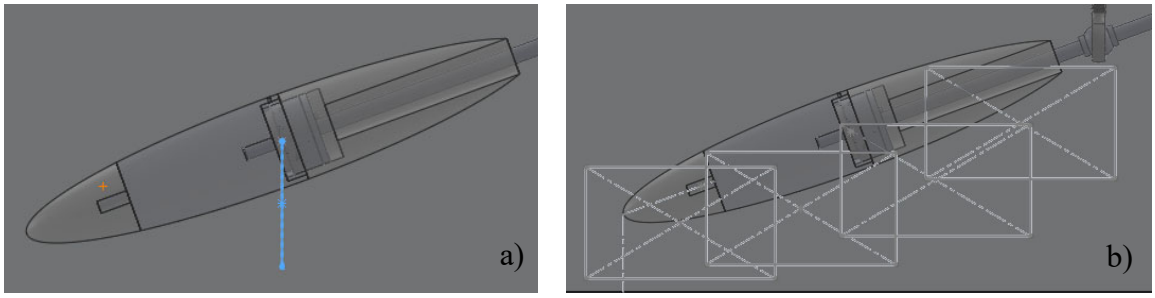

Figure 9: (a) Laterally-oriented field of view (perpendicular to the inflow) and (b) longitudinally-oriented field of view (parallel to inflow). The longitudinal fields of view will be overlapped as shown to cover the entire near-body flow field. Flow is from left to right.

The laser was aligned using the following procedure. The laser head is mounted beneath the tunnel and the beam is horizontal and parallel to the tunnel. The beam is directed upward into the tunnel using a 90° mirror. First, the 90° mirror was made level using an inclinometer with 0.1° resolution. Next, a plumb bob was hung from the lid of the tunnel and allowed to come to rest over the

observation glass of the floor of the tunnel. A small target with a 5 mm hole was placed on the underside surface of the observation glass. The laser was fired in alignment mode up through the target to the lid. The breadboard (to which the cameras and laser optics were attached) was translated until the beam went through the target hole and hit the lower surface of the lid at the point where the plumb bob hung. Minor adjustments were made by rotating the 90° mirror until vertical alignment was achieved. A midline mark was scribed on the bottom of the lid, and the SPIV system was traversed, with the laser firing in alignment mode to ensure the SPIV system path and tunnel lid were aligned (i.e. the beam struck the centerline of the lid along the entire traverse from upstream to downstream). The spheroid was then placed in the tunnel and the SPIV sled was again traversed from upstream to downstream with the laser firing in alignment mode to ensure the beam was aligned with the major axis of the body. Once alignment was verified, the beam forming optics were installed above the 90° mirror. The SPIV system was again translated from upstream to downstream with the laser firing in alignment mode, this time with the beam formed into a thin sheet, to ensure the sheet was aligned with the symmetry plane of the body.

The seed particles used in the present experiment are Potters Industries Sphericell hollow glass spheres with a mean diameter of 12 μm and a density of 1.05 kg/m^3. Seed particles were added to the tunnel water until the flow was slightly cloudy, reminiscent of grapefruit soda. Upon analysis, if the ratio of good vectors to bad vectors was low, additional seed particles were added approximately 8 oz. at a time. A mixture of 1 part particles to 3 parts water was added to a household blender, along with a few drops of dish soap as a surfactant to help break up the large clumps of seed. A compromise is made between seeding density, which improves image correlation, and water opacity, which is reduced as seeding density increases.

2.6. **Orientation of Flow Fields**

The coordinate system for the present experiment is as follows. The origin is taken to be the nose of the body in all orientations, longitudinal and lateral. The streamwise direction, x extends downstream from the nose toward the tail and sting, parallel to the flow (as opposed to the body). The vertical coordinate, y is oriented vertically upward. The z-axis is therefore directed out of the page.

Each individual field of view is insufficient in size to cover the regions of interest over the entire body; therefore, it is necessary to make measurements at multiple overlapping fields of view and orient them to cover the entire region of interest, an example of which is shown in Figure 10 for the spheroid at 20° of inclination with fields of view oriented longitudinally to the body.

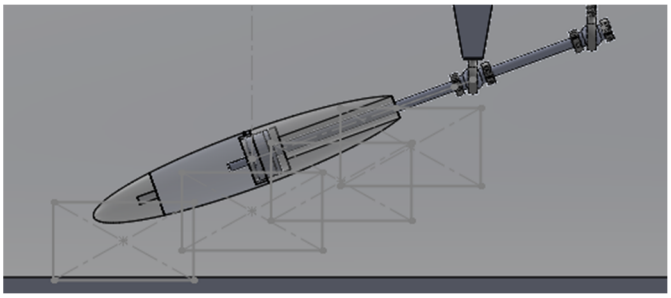

Figure 10: A schematic showing the longitudinal orientation of the fields of view relative to the body.

This was accomplished using the calibration target board. The target board was placed in the streamwise direction (Figure 11a) using an alignment laser that is fixed to the same breadboard as the cameras and PIV laser. The alignment laser was first aligned with the tip of the spheroid. This location was taken to be $x = 0$. From this reference, the downstream location was measured using a laser distance measurer with a resolution of 100 μm. The calibration target was then adjusted to the appropriate vertical height and the cameras raised to the same height. The flow field was reconstructed by translating the coordinates of each field of view according to the measured downstream distance and height above the tunnel floor.

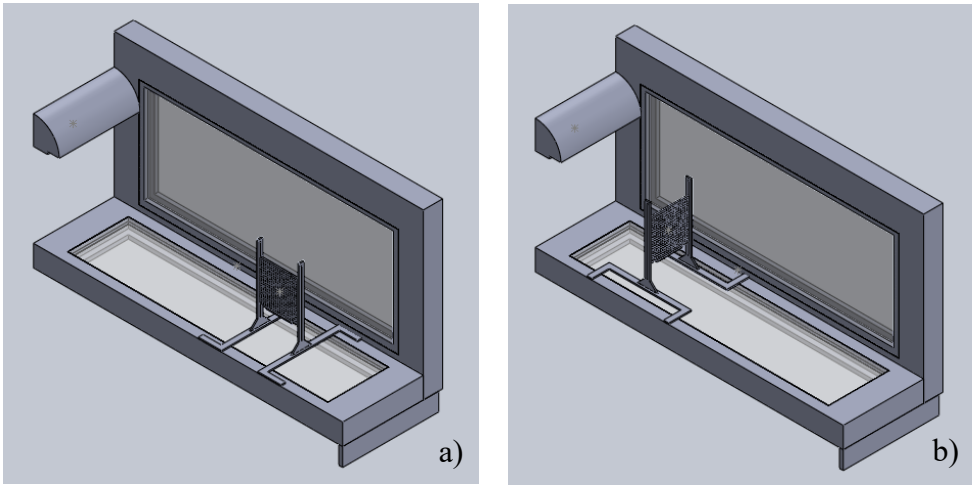

Figure 11: Target board position in the a) longitudinal orientation and b) in the lateral orientation. The vertical legs of the fixture allow the target board to be raised relative to the tunnel floor. The "feet" of the fixture ensure repeatable placement of the target board relative to the tunnel wall in both the longitudinal and lateral orientations.

For fields of view in the lateral orientation, the target board was placed perpendicular to the mean flow, as shown in Figure 11b. The streamwise position of the target was set to x/L of 0.6, 0.7, 0.8, and 0.9 relative to the nose of the body, taken to be x/L of 0. Lateral fields of view are oriented such that the observer is downstream of the field of view, facing upstream (in the negative streamwise direction) shown in Figure 12.

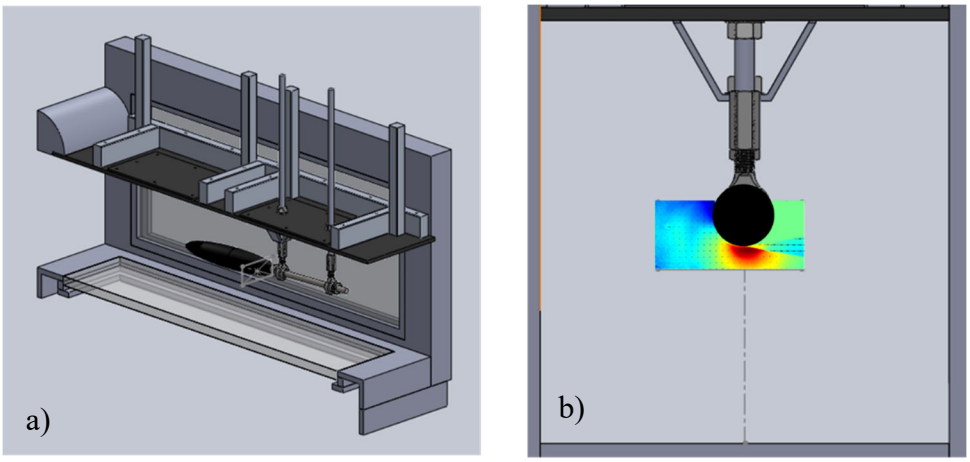

Figure 12: Field of view orientation relative to the body in the lateral orientation (shown as a gray rectangle) (a), shown relative to how it is viewed in subsequent figures (viewed from downstream, looking upstream in the -x direction (b).

2.7. **Calculation of the Mean Flow, Vorticity, and Turbulence Statistics**

In order to calculate the mean flow, U a sufficient number of realizations must be recorded such that the average value at each point in space converges. According to the Reynolds decomposition:

$$u = U + u' \tag{7}$$

where u is the instantaneous velocity observed at some point in space and time (within the field of view), U is the mean velocity at any point in the field of view, and u' is the fluctuating component of the velocity. In other words, the instantaneous velocity is the sum of a mean velocity plus a fluctuating component. Averaged over a sufficient number of realizations, the instantaneous velocity at particular point in the flow field converges to a single value, the mean flow:

$$\frac{1}{N}\sum_{i=1}^{N} u_i = U \tag{8}$$

Related to this, over some number of realizations, the average of the fluctuating velocity goes to 0:

$$\frac{1}{N}\sum_{i=1}^{N} u_i{}' = 0 \tag{9}$$

From the mean flow, the vorticity, ζ a measure of flow rotation, can be calculated for the direction normal to the measurement plane. For example, for lateral fields of view, the streamwise vorticity is calculated as follows:

$$\zeta = \nabla \times \mathrm{V} = \left(\frac{\partial w}{\partial y} - \frac{\partial v}{\partial z}\right)\hat{\imath} \tag{10}$$

In addition to mean flow and vorticity measurements, turbulence statistics can be calculated, first by calculating the fluctuating velocity from Equations 3 and 4:

$$u' = u - U \tag{11}$$

From the fluctuating velocity in each of the three Cartesian directions, all six unique components of the Reynolds stress tensor can be calculated:

$$u_i'u_i' = \begin{bmatrix} -u'u' & -u'v' & -u'w' \\ -v'u' & -v'v' & -v'w' \\ -w'u' & -w'v' & -w'w' \end{bmatrix} \tag{12}$$

The diagonal terms, $-u_i'u_i'$ are representations of the turbulence kinetic energy and the non-diagonal terms, $-u_i'u_j'$ are called the Reynolds stress and are associated with momentum transport. The Reynolds stress tensor is symmetric, thus $-u_i'u_j' = -u_j'u_i'$.

3. Results

3.1. **Mean Flow, Vorticity, and Turbulence Measurements**

Velocity field measurements have been made in the longitudinal and lateral orientations at angles of incidence of 2.5°, 5°, 10° and 20°, at Reynolds numbers of 1, 2, and 3 × 10^6. The longitudinal orientation spans the entire length of the spheroid as shown in Figure 10. In the lateral orientation, shown in Figure 12, data is taken at four different stations, x/L = 0.6, 0.7, 0.8, and 0.9. At each of these configurations, mean flow fields in the x (streamwise), y (vertical), and z (out of the page), and directions have been processed and plotted along the body of the spheroid. All of the mean flow plots in the longitudinal and lateral configurations can be found in Appendix A-P.

The three parameters varied in each of the following measurements were length-based Reynolds number, presence of the boundary layer trip (referred to as *smooth* for the untripped body, and *tripped* for the body with the boundary layer trip), and angle of inclination. The following discussion is organized by examining the impact on the flow field by varying these parameters.

When examining the effect of varying the Reynolds number in the longitudinal orientation, the vertical component of the velocity will be primarily looked at as it is the most dynamic and revealing of the parameter variation. First, Figure 13, which shows the mean vertical velocity, normalized by the free-stream velocity, shows the effect of varying Reynolds number at 2.5° of inclination, in the tripped configuration.

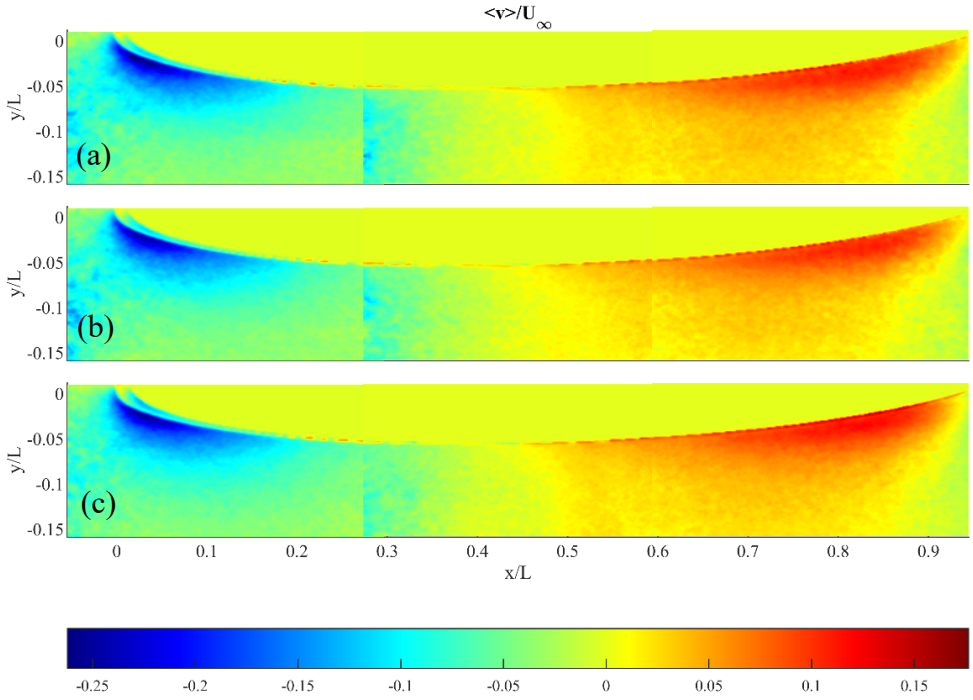

Figure 13: Mean velocity v, at $\alpha = 2.5°$ and Re_L of 1×10⁶ (a), 2×10⁶ (b), and 3×10⁶ (c) (tripped).

The tripped configuration was selected because its results are more widely applicable and more easily compared between different models. The color range for all plots is the same, taken from the range of normalized velocities for the 3×10^6 case.

At all three Reynolds numbers, the stagnation point is prominently located at the nose of the spheroid, and has the same relative negative intensity. In the 2.5° configuration, there is minimal change in the vertical component of the mean velocity as Reynolds number increases. Similarly, the vertical velocity maxes out at approximately 15% of the streamwise velocity at all three Reynolds numbers. Looking at the wake topology in all three cases, it appears as though the separated region remains fixed, in terms of size and position, for all three Reynolds numbers. Figure 14 shows results from the same parameters discussed above in Figure 13, but in the lateral orientation.

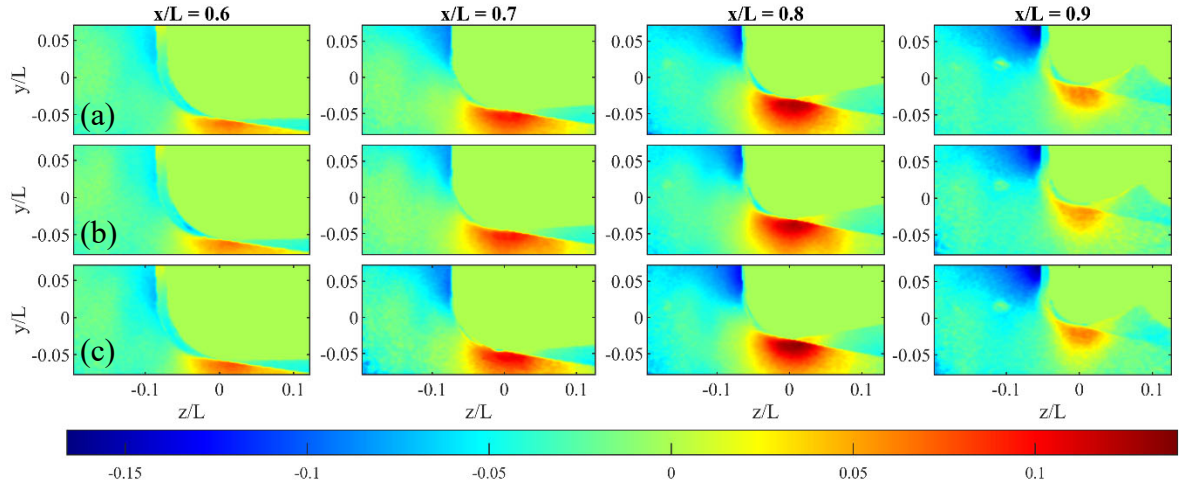

Figure 14: Mean velocity v, at $\alpha = 2.5°$ and Re_L of 1×10^6 (a), 2×10^6 (b), and 3×10^6 (c) (tripped).

The results shown in Figure 14, in the lateral orientation, agree with the longitudinal results shown in Figure 13. As Reynolds number increases, the vertical velocity profile does not vary considerably. The lateral fields of view in Figure 14 confirm that the wake of the spheroid at 2.5° is greatest in both size and intensity at approximately $x/L = 0.8$. Moving downstream of $x/L = 0.8$, the wake dissipates in both size and intensity, shown in the $x/L = 0.9$ fields of view.

Figure 15 shows the effect of varying Reynolds number but at an angle of inclination of 20° and in the longitudinal orientation, all other parameters remaining the same.

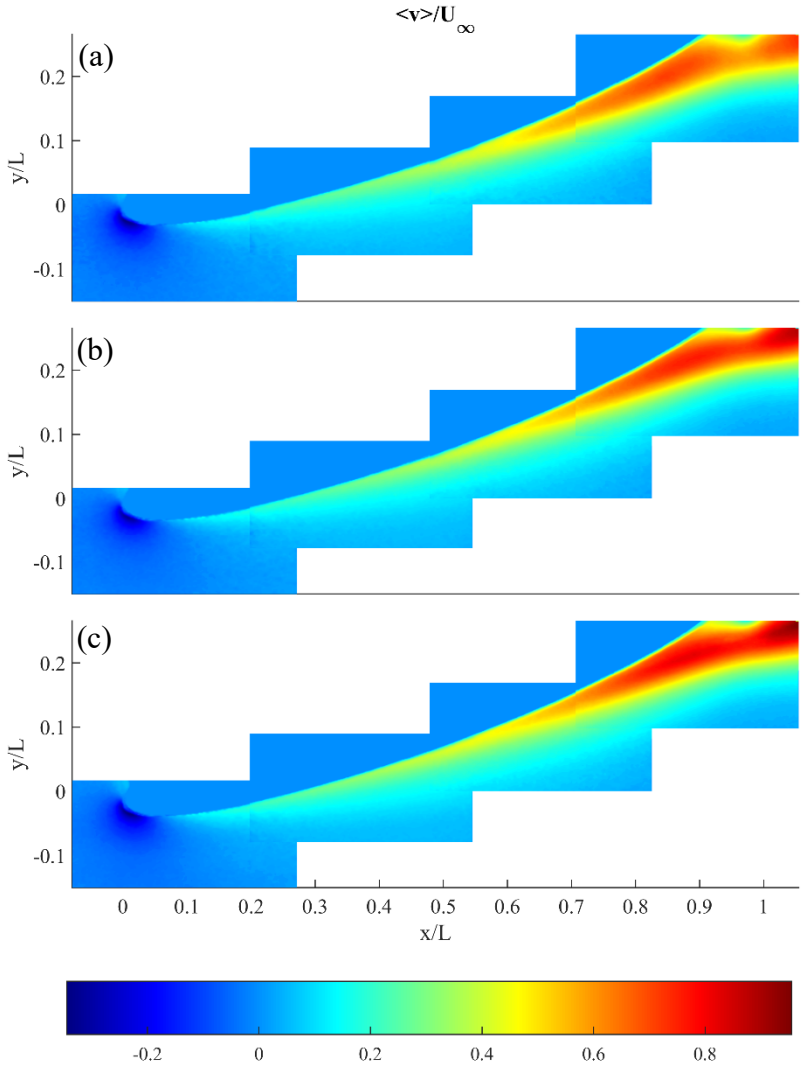

Figure 15: Mean velocity v, at $\alpha = 20°$ and Re_L of 1×10⁶ (a), 2×10⁶ (b), and 3×10⁶ (c) (tripped).

Similar to in the 2.5° case, the stagnation point is prominently located at the nose of the spheroid, and the vertical velocity does not change drastically from a Reynolds number of 1 to 3×10^6. The relative intensity of the vertical velocity in the wake of the spheroid does increase as Reynolds number increases, as indicated by the darker red in the wake of the spheroid. The variation in the flow field with increasing Reynolds number agrees with Ahn and Simpsons findings, which state that there is a critical Reynolds number of roughly 2.5×10^6 [3]. In this data set, there is only one configuration above this critical Reynolds number, so the anticipated result of variation in the flow fields at each different Reynolds number is met. Due to the resolution of the velocity measurements, the separation point/line cannot be determined with high fidelity. Although the exact location of separation cannot be determined, separation does not seem to vary much with increasing Reynolds number, perhaps moving slightly upstream when comparing 1×10^6 to 3×10^6 Reynolds number. This also agrees with the findings of Ahn and Simpson [3]. Figure 16 shows results from the same parameters discussed above in Figure 15, but in the lateral orientation.

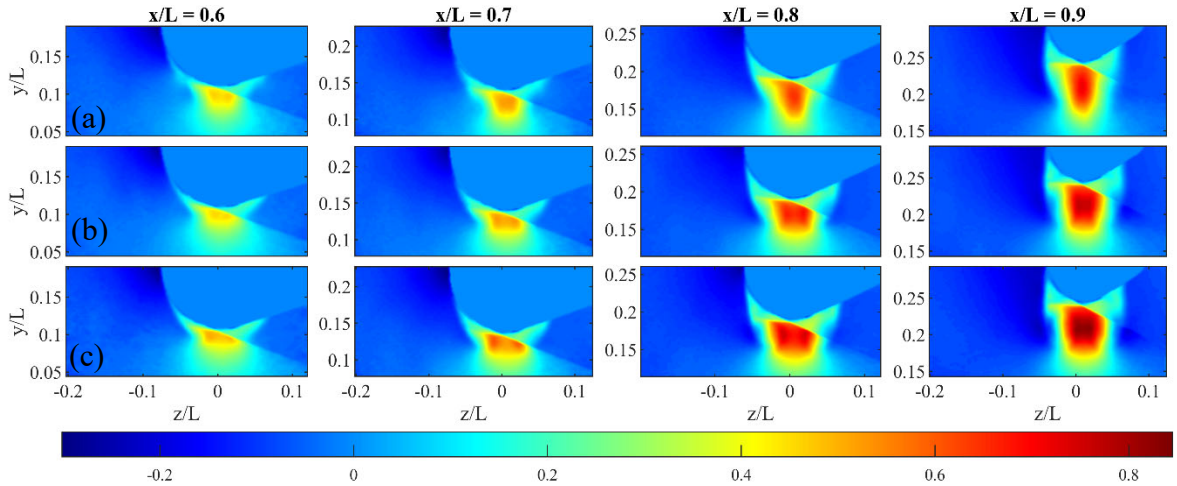

Figure 16: Mean velocity v, at $\alpha = 20°$ and Re_L of 1×10⁶ (a), 2×10⁶ (b), and 3×10⁶ (c) (tripped).

As seen in Figure 16, as Reynolds number increases, the relative intensity of the vertical velocity increases, across all lateral stations. The increase in the relative magnitude of the vertical velocity as Reynolds number increases is especially prevalent at $x/L = 0.9$. Also, unlike in the 2.5° case, the vertical size of the wake increases moving from a position of $x/L = 0.8$ to 0.9. This indicates that at an angle of inclination of 20°, the wake is strong enough that the free stream does not force the wake to shrink again before traveling the full length of the spheroid.

Another parameter which displays the effects of varying Reynolds number at 20° is the vorticity, calculated using Equation (10), which describes the amount of rotation in the wake. Figure 17 shows vorticity in the wake of the spheroid at 20° and varying Reynolds numbers.

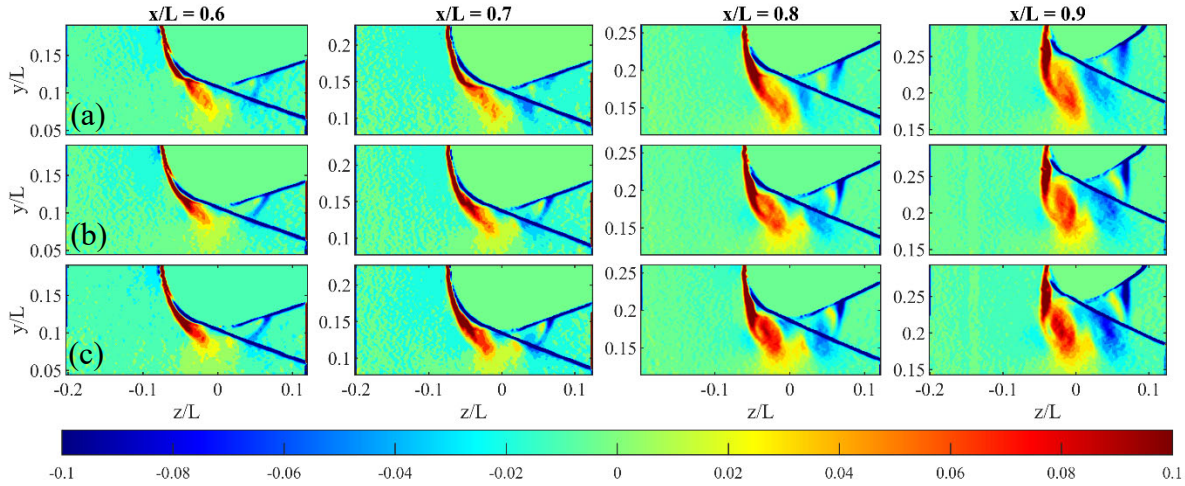

Figure 17: Vorticity ζ, at $\alpha = 20°$ and Re_L of 1×10⁶ (a), 2×10⁶ (b), and 3×10⁶ (c) (tripped).

Similar to what was seen in earlier figures, in Figure 17, as Reynolds number increases, the vorticity intensity increases as well. The counter-rotating vortices, indicated by the positive red and negative blue, are strongest and most developed at the $x/L = 0.9$ position. The increase in vorticity with increasing Reynolds number is most apparent at the $x/L = 0.8$ position. This result agrees with Barber and Simpson's findings, in which they saw vorticity increase with increasing

Reynolds number, but at an angle of inclination of 15° [2]. Additionally, Barber and Simpson found that vortical flow in the wake of the spheroid increases moving downstream, and the center of vortical flow moves further from the spheroid radially moving downstream [2]. The results seen in Figure 17 show strong agreement to these findings.

The Reynolds stress, particularly the in-plane component, $-v'w'$ is illustrative of the variation with Reynolds number. Figure 18 shows $-v'w'/U_\infty^2$ for Re = 3 $\times 10^6$ at an angle of 20° at a downstream distance of x/L = 0.9 for the tripped body.

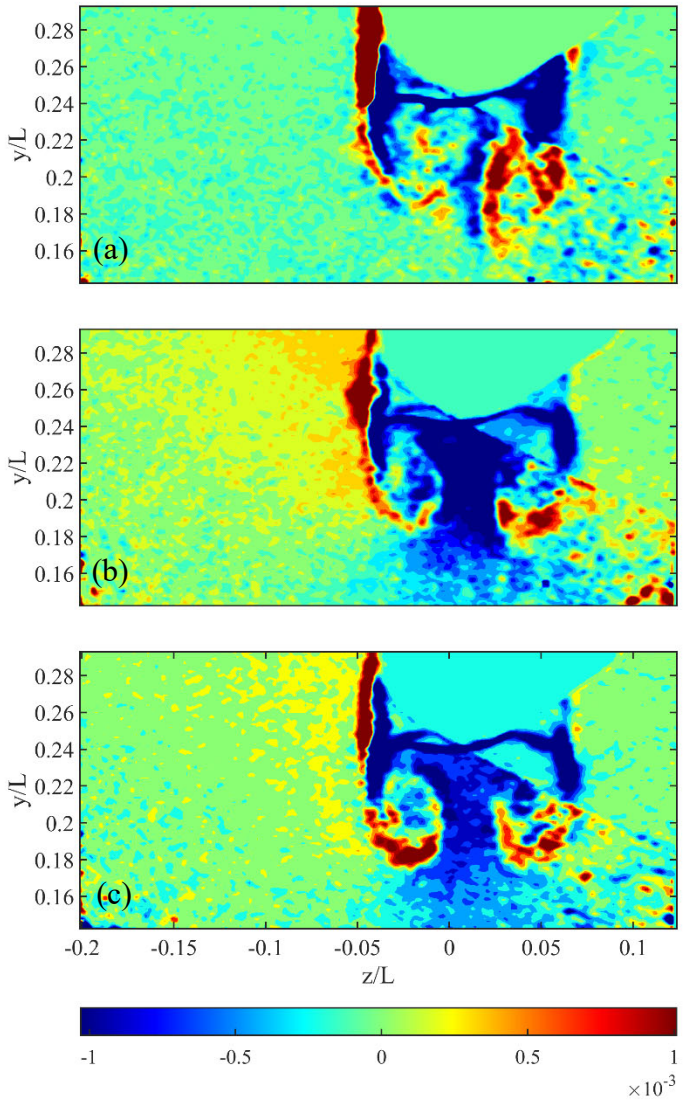

Figure 18: Reynolds shear stress, $-v'w'/U_\infty^2$ for Reynolds number of 1×10⁶ (a), 2×10⁶ (b), 3×10⁶ (c). All figures are plotted using the same colorbar range.

The Reynolds stress indicates the turbulent transport of momentum. For example, in Figure 18c it shows momentum being transported into the wake by the counter-rotating vortices. Taken together, the three figures show an increase in the coherency with Reynolds number, with the vortices being more well-defined and positionally stable in the 3×10⁶ case (Figure 18c).

In Figure 19, the spheroid is in the tripped configuration for the reasons previously discussed. The Reynolds number is set to 1×10^6 at all angles of inclination, ranging from 2.5° to 20°.

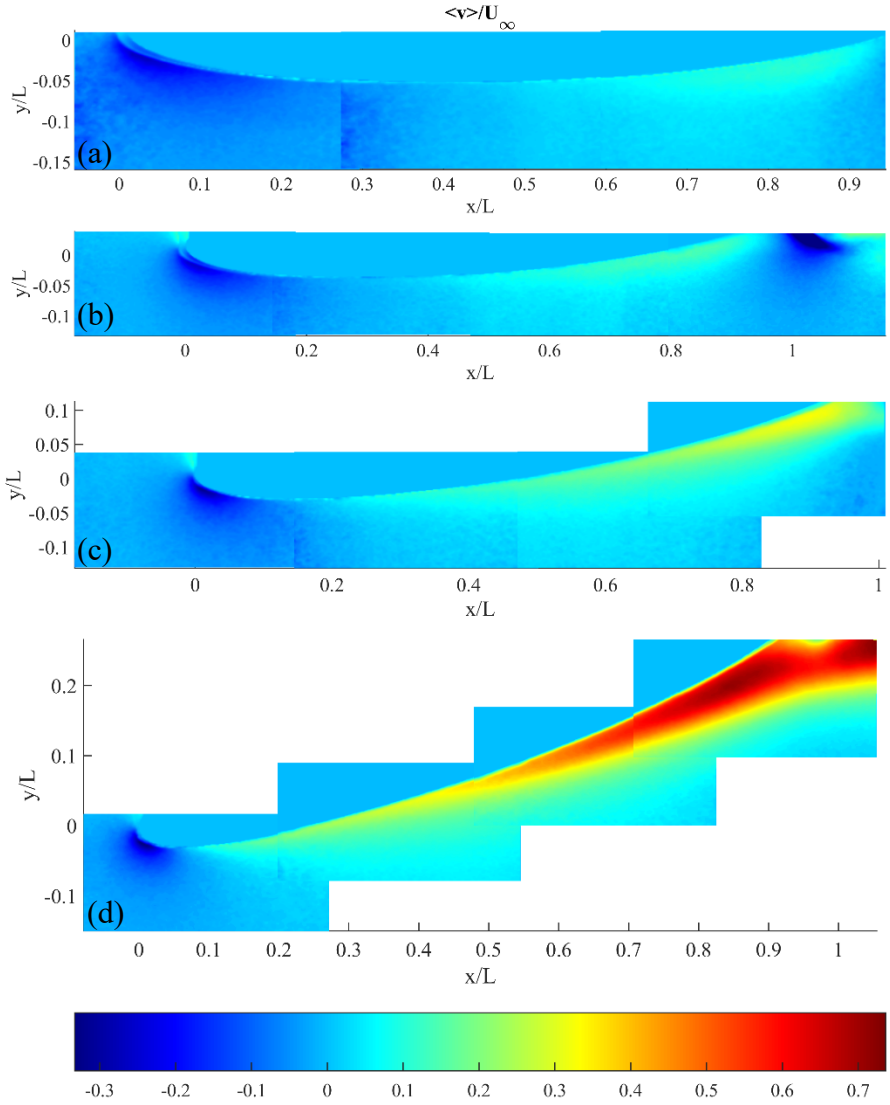

Figure 19: Mean velocity v, at $\alpha = 2.5°$ (a), $5°$ (b), $10°$ (c), and $20°$ (d), and Re_L of 1×10^6 (tripped).

Looking at Figure 19, the wake topology across all angles of incidence is similar in shape and size. The intensity of the vertical velocity in the wake is what varies greatly between the different angles of incidence. At an angle of 2.5°, the vertical velocity component reaches approximately 15% of the streamwise velocity, whereas at an angle of 20°, the vertical velocity component reaches over 70% of the streamwise velocity. Although the specific location of separations cannot be determined at this point in time, it is evident that separation travels upstream as angle of inclination increases, showing strong agreement with Ahn and Simpson's findings [3].

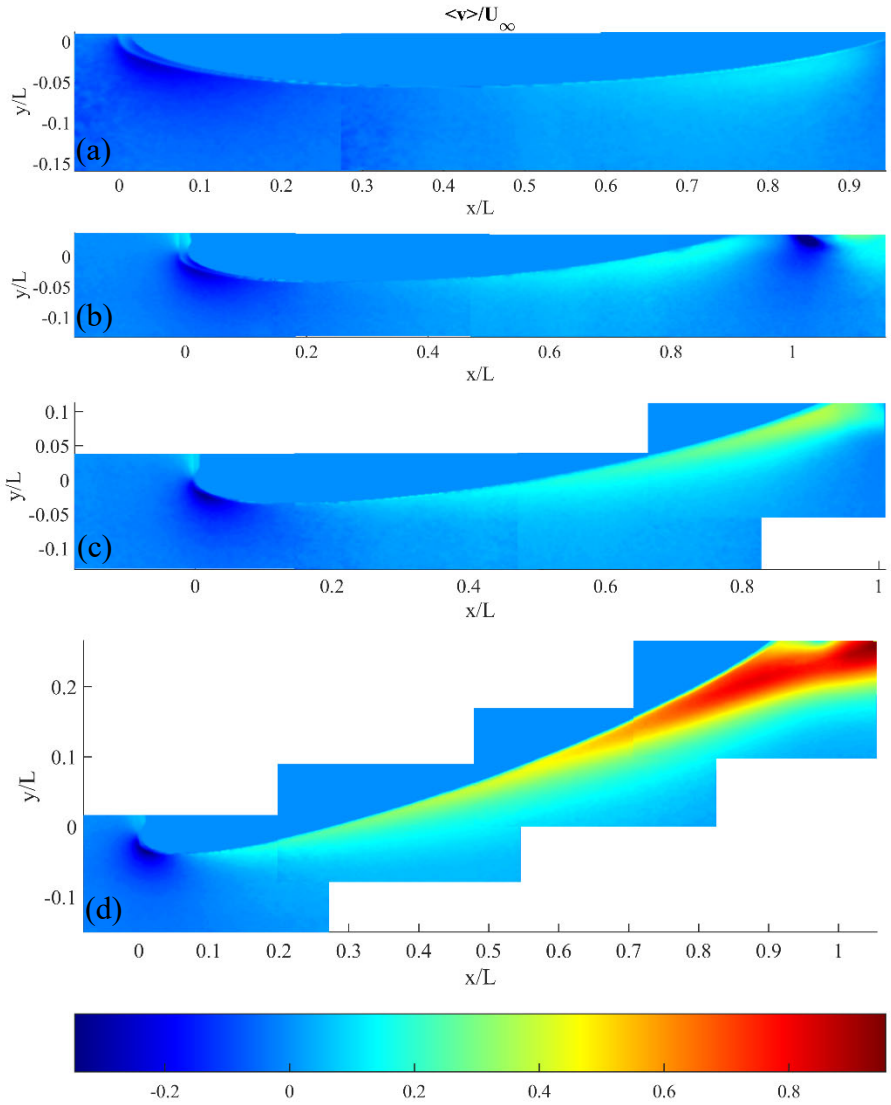

Figure 20: Mean velocity v, at $\alpha = 2.5°$ (a), $5°$ (b), $10°$ (c), and $20°$ (d), and Re_L of 3×10^6 (tripped).

When varying angle of inclination at a higher Reynolds number of 3×10^6, the results are similar to what is seen at a Reynolds number of 1×10^6. The wake topology, in regards to size and shape, is similar across all angles. The difference in the intensity of the wake is even greater than what was seen at 1×10^6 Reynolds number. In Figure 20, at 2.5°, the wake is nearly unidentifiable when held to the same scale as the 20° case. At 5°, the formation of the wake becomes more visible, as indicated by the light blue in the aft end of the body. Transitioning to 10° and 20°, the wake is far more visible, similar to what was seen in Figure 19. A primary difference between the wakes in Figure 19 and Figure 20, is that at higher Reynolds numbers (Figure 20) the wakes across all angles of attack appear to be more condensed, remaining closer to the body of the spheroid.

The streamwise velocity in the lateral orientation at a Reynolds number of 3×10^6 also displays the effect of varying angle of inclination and is shown in Figure 21.

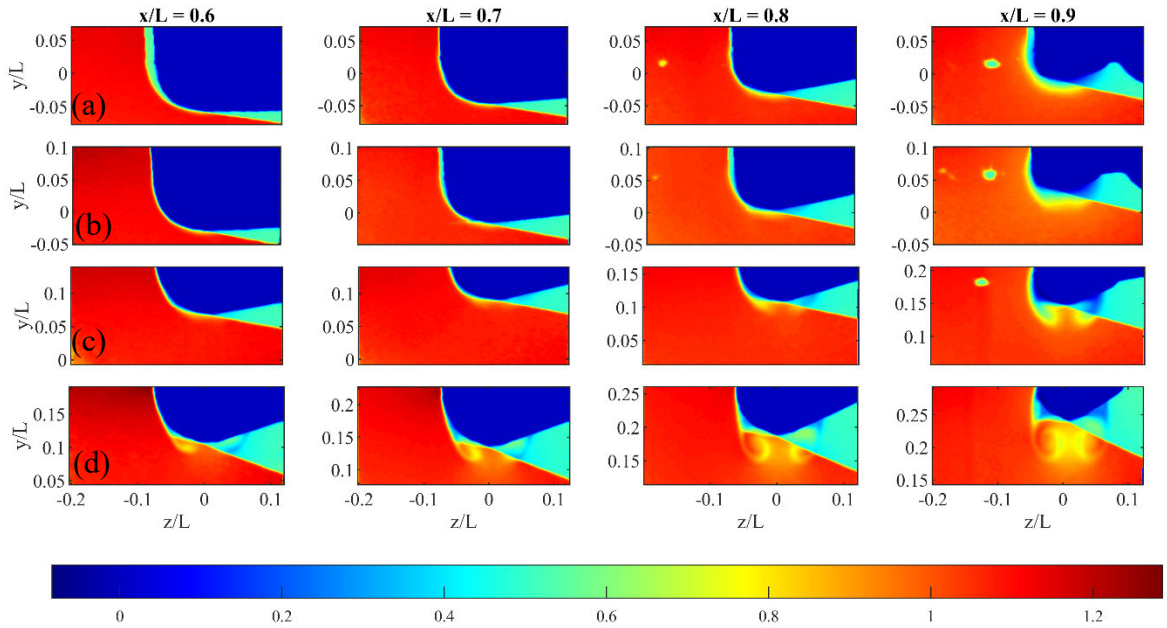

Figure 21: Mean velocity u, at $\alpha = 2.5°$ (a), $5°$ (b), $10°$ (c), and $20°$ (d), and Re_L of 3×10⁶ (tripped

Looking at the streamwise velocity profiles in Figure 21, it is evident that angle of inclination has a large impact on separation, and its location along the body of the spheroid. Looking at the 2.5° case, separation is not observed until the $x/L = 0.8$ position, indicated by the yellow coloring barely extending into the free stream. At 20°, there is clear separation at $x/L = 0.6$, shown by the beginnings of the formation of two counter rotating vortices, which by $x/L = 0.9$, are prominently evident. This shows strong agreement with the findings of Goody, Simpson, and Engel, who found that at an angle of inclination of 20° and a Reynolds number of 4.2×10^6, there is strong separation and the flow exhibits a high degree of three-dimensionality [5]. Overall, Figure 21 confirms the findings in Figure 19 and Figure 20 which show that separation moves up stream with increasing angles of inclination.

Vorticity is also used to show the effects of varying angles of inclination, and the results are shown in Figure 22.

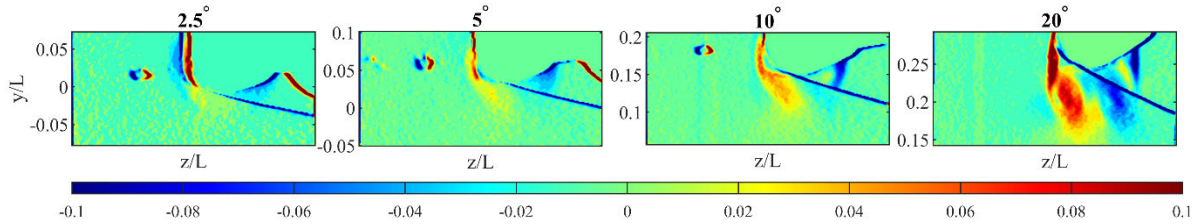

Figure 22: Vorticity ζ, at $\alpha = 2.5°$, $5°$, $10°$, and $20°$, x/L = 0.9, and Re_L of 3×10⁶ (tripped).

In Figure 22, vorticity is affected by increasing angle of inclination similarly to mean velocity. At an angle of inclination of 2.5°, there is nearly no identifiable vorticity, or angular rotation, in the wake of the spheroid. Moving to 20°, with Reynolds number and position along the body remaining constant, two counter rotating vortices are clearly present. This confirms trends found in previous results, now applied to vorticity, that vorticity in the wake of the spheroid increases as

angle of inclination increases. Additionally, these results also agree with Fu et al., who similarly found that the strength of vortices increased with increasing angle of inclination [4].

Figure 23 examines the effect of tripping at low angles of inclination, and varying Reynolds numbers. Low angles of inclination are used because it is anticipated that tripping will have a greater effect at lower angles of inclination. Figure 23 shows the spheroid in the tripped and smooth configurations at an angle of inclination of 2.5° and a Reynolds number of 1×10^6.

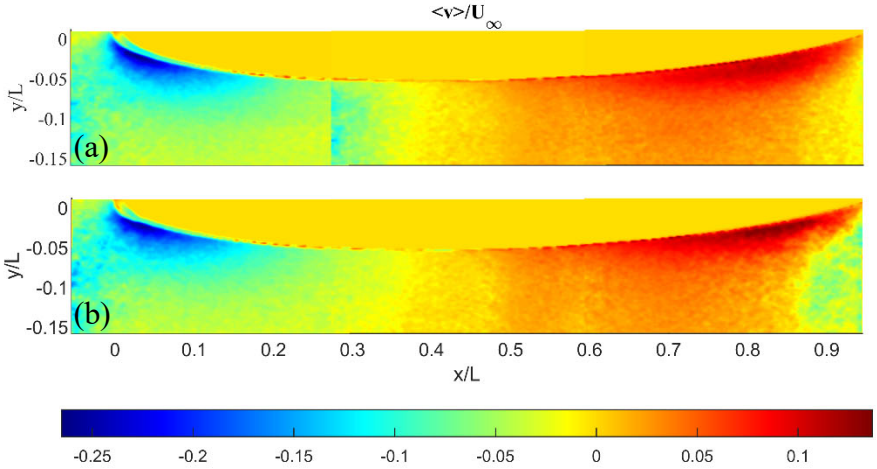

Figure 23: Mean velocity v, at tripped (a) and smooth (b) and $\alpha = 2.5°$ and Re_L of 1×10^6.

Comparing the tripped and smooth cases in Figure 23, the wake topology is very similar. The main difference between the two configurations is that the intensity of the vertical velocity in the wake of the smooth case appears to be greater than that in the tripped case. It should be noted that the scale in Figure 23 is smaller than in past figures, therefore magnifying any differences between the two cases. To further examine and validate the results found in Figure 23, the lateral results using the same parameters are shown in Figure 24.

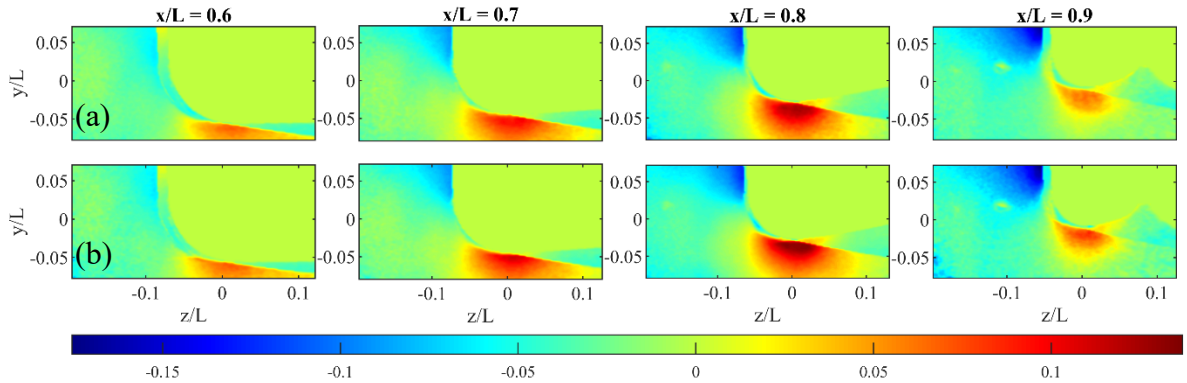

Figure 24: Mean velocity v, at tripped (a) and smooth (b) and $\alpha = 2.5°$ and Re_L of 1×10^6.

In Figure 24, the mean flow in the vertical direction is nearly identical in the tripped and smooth configurations at $x/L = 0.6$ and 0.7. At $x/L = 0.8$ and 0.9, the vertical velocity shed into the wake of the smooth case appears to be slightly larger in magnitude. This agrees with what was observed in the longitudinal images shown in Figure 23. Figure 25 displays the same parameters shown in Figure 23, but at a Reynolds number of 3×10^6.

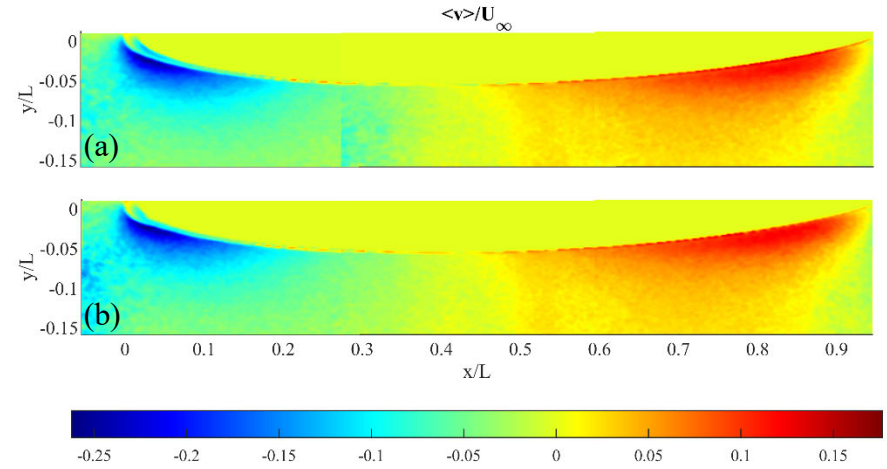

Figure 25: Mean velocity v, at tripped (a) and smooth (b) and $\alpha = 2.5°$ and Re_L of 3×10^6.

Even more so than in Figure 23, the vertical velocity profiles between the two cases in Figure 25 are nearly identical. The relative vertical velocity is greater at a Reynolds number of 3×10^6 than it was at a Reynolds number of 1×10^6 in both the tripped and smooth configurations.

Figure 26 shows the spheroid in the tripped and smooth configurations at an angle of inclination of 5° and a Reynolds number of 1×10^6.

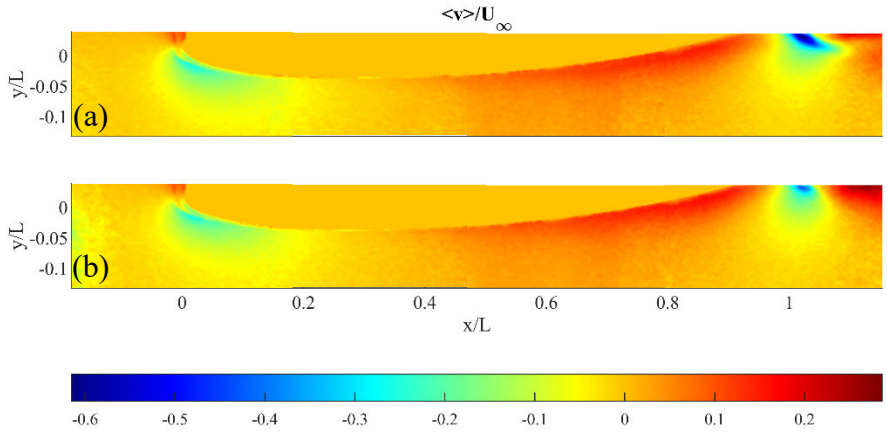

Figure 26: Mean velocity v, at tripped (a) and smooth (b) and $\alpha = 5°$ and Re_L of 1×10^6.

As was the case in examining the effect of trip at an angle of inclination of 2.5°, the trip appears to have minimal impact in the vertical velocity profile, as shown in Figure 26. Small differences in the wake topology can be observed, but further examination in the lateral orientation, shown in Figure 27, using these same parameters is required to further examine if the trip has any effect.

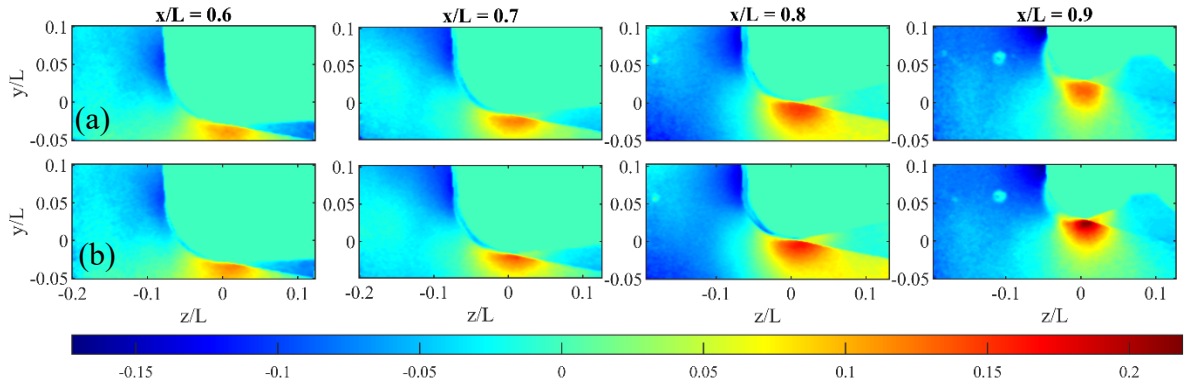

Figure 27: Mean velocity v, at tripped (a) and smooth (b) and $\alpha = 5°$ and Re_L of 1×10⁶.

Looking at the tripped and smooth vertical velocity in the lateral orientation at 5°, it is apparent that tripping has little to no impact on the profile of the vertical velocity. At the station $x/L = 0.9$, there does appear to be a difference between the tripped and smooth cases. Upon further examination of the lateral and longitudinal results at 5°, located in Appendices C, D, K and L, it is concluded that the differences observed at the $x/L = 0.9$ station are due to measurement or processing error, and are not physical. More specifically, in Appendix K, the vertical velocity at a Reynolds number of 1×10^6, is greater in relative magnitude than the vertical velocity seen at Reynolds numbers of 2 and 3×10^6. This does not agree with the trend seen across all mean flow data, suggesting that the results seen in Figure 27 at $x/L = 0.9$ are due to some sort of measurement or processing error. Figure 28 shows the effect of trip on vorticity at an angle of inclination of 20°.

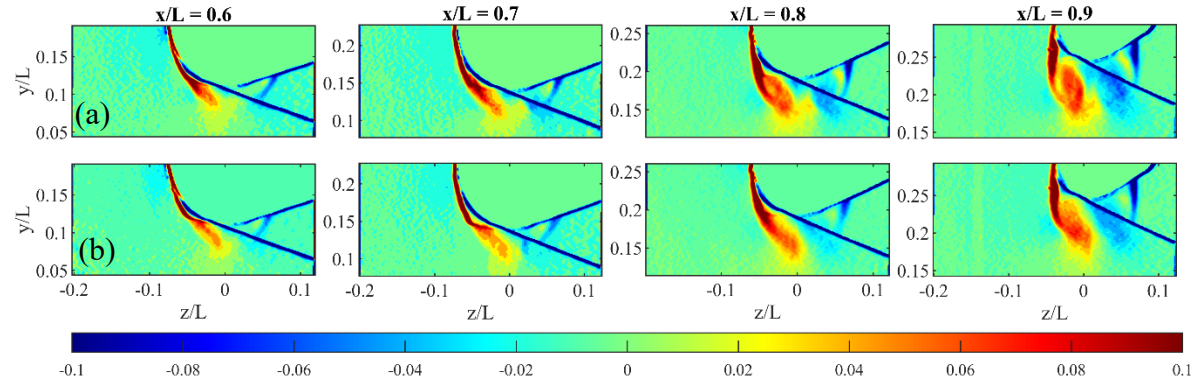

Figure 28: Vorticity ζ, at tripped (a) and smooth (b), and $\alpha = 20°$, and Re_L of 2×10⁶.

Similar to previous results involving the effect of trip, tripping does not appear to have a large impact on vorticity. Especially at an angle of inclination of 20°, where separation and turbulence are introduced early, it is anticipated that trip would have a minimal impact on the flow in the wake of the spheroid. However, at the $x/L = 0.8$ and 0.9 stations, the vortices appear to be more developed, in size and magnitude, in the tripped configuration. Fu et al. found that their trip configuration, at a Reynolds number of 2.1×10^6, resulted in vorticity being spread over a wider area, which shows strong agreement with the results seen in Figure 28 [4]. Further observation at stations further upstream is necessary in order to determine if the trip causes turbulence at an earlier position, or simply accelerates the wake development in this configuration.

The in-plane Reynolds shear stress is also helpful in illustrating the differences between the smooth and tripped case. Figure 29 shows $-v'w'/U_\infty^2$ for Re = 3 $\times 10^6$ at an angle of 20° at a downstream distance of x/L = 0.9 for the smooth (left column) and tripped (right column) body.

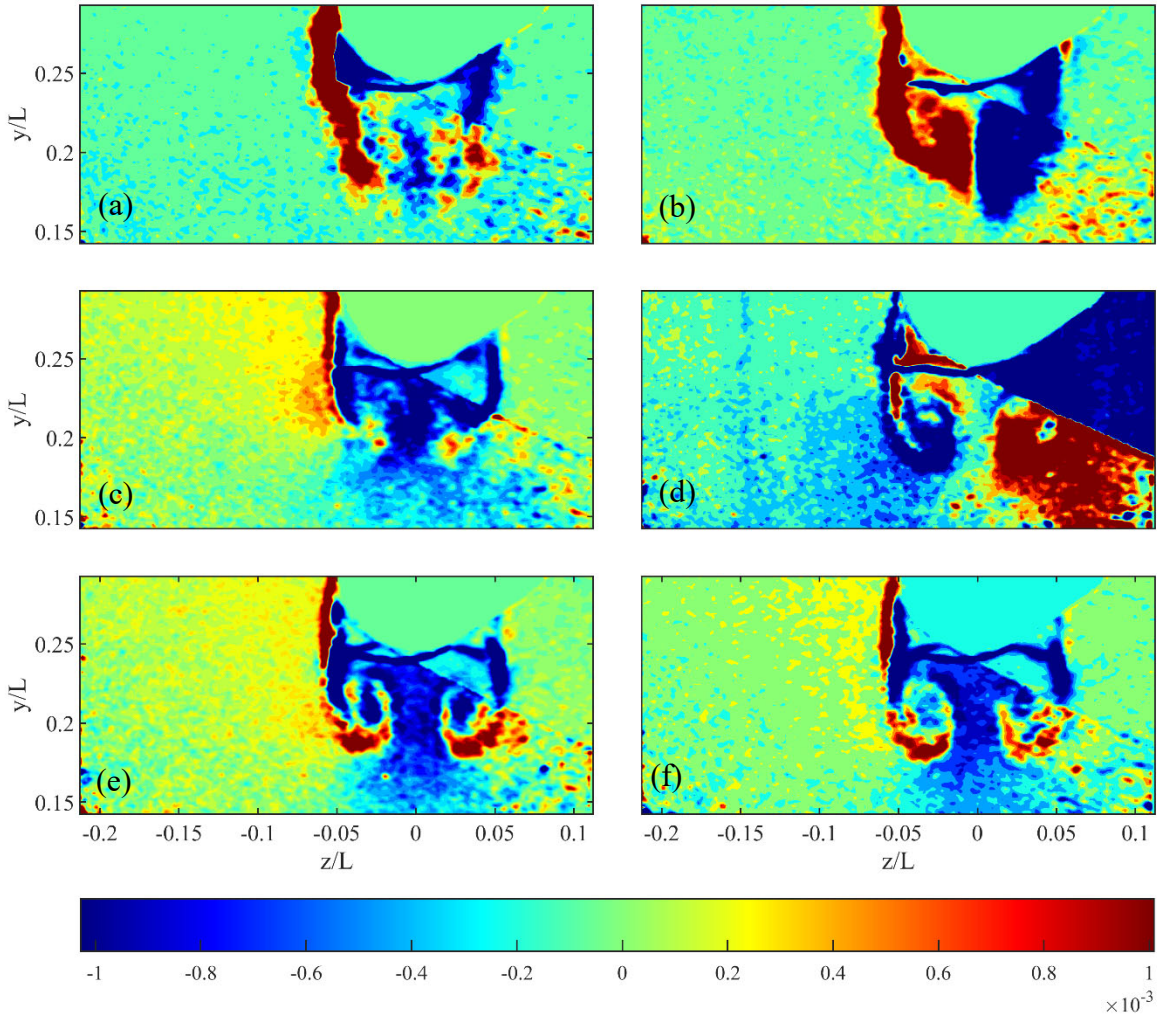

Figure 29: Reynolds shear stress, $-v'w'/U_\infty^2$ for Reynolds numbers of 1, 2, and 3×10⁶ (rows) at 20° and x/L of 0.9 for the smooth (left column) and tripped (right column). All figures are plotted using the same colorbar range.

The purpose of the trip is to induce the flow field to behave similarly over a range of Reynolds numbers. The similarity between Figure 29e and f indicates that for the body at 20°, the flow field is fully turbulent by 3×10⁶ in either case, smooth or tripped. However, there is significant variation in the flow field for the smooth body over the range of Reynolds numbers (Figure 29a, c, and e). Though there is *some*, there is *less* variation over the same range for the tripped body (Figure 29b, d, and f) indicating that the trip is having some effect.

3.2. **Convergence of First and Second-Order Statistics**

In order to ensure that the number of realizations taken at each configuration is sufficient to allow the average of the fluctuating velocity to converge to 0, the fluctuating velocity is plotted for each Cartesian coordinate velocity, averaging 25, 50, 75, and 100 realizations, respectively. The field of view shown in Figure 30 is for the furthest downstream field of view for the highest Reynolds number and highest angle of inclination, assumed to be the most turbulent field of view.

The fluctuating portion of the velocity shown in Figure 30, is solved for using Equation (8). Due to the random nature of the fluctuating velocity, when summing the fluctuating velocity across multiple realizations, as the number of realizations increases, the sum converges to zero. The scale used in Figure 30 is 1% of the extreme values of the fluctuation (e.g. $\max(u')/100$), in order to ensure proper convergence is reached. At 25 realizations the plots do not converge, but by 125 realizations the fluctuating velocities have converged to approximately zero, as indicated by the solid color in those plots. This suggests that 125 realizations is sufficient to provide a converged spatial average for the first-order statistics.

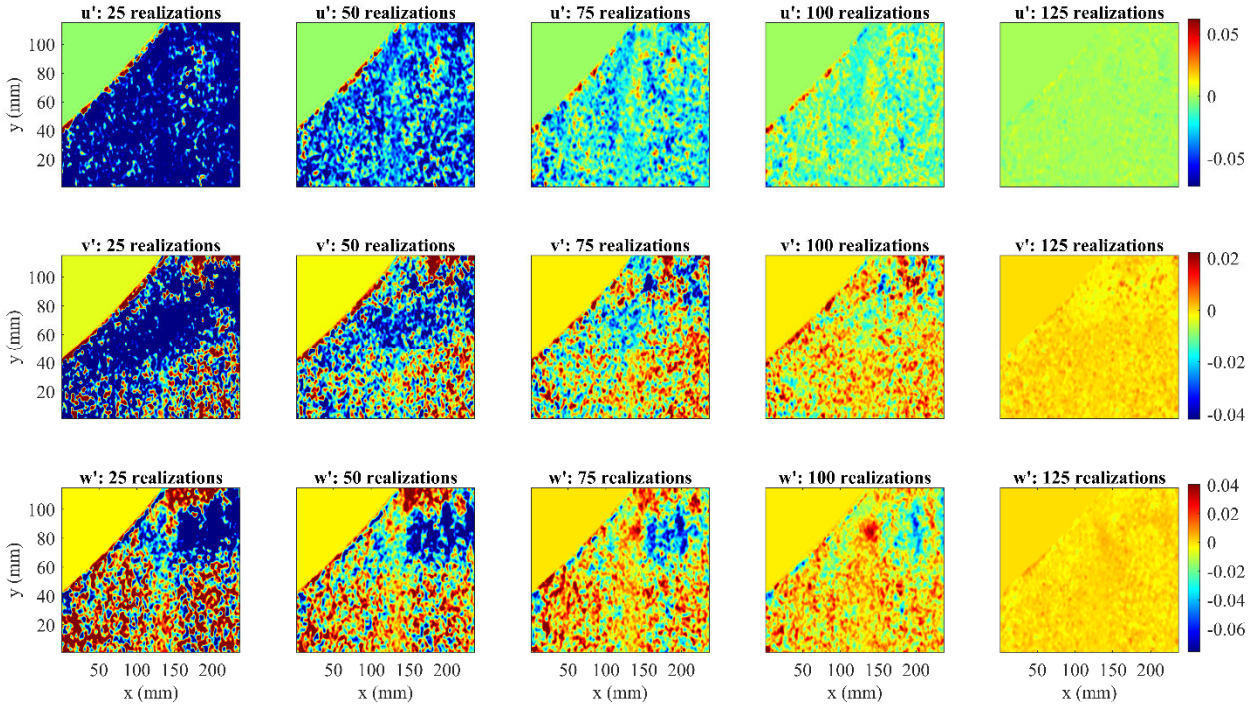

Figure 30: Average over 25 (first column), 50 (second column), 75 (third column), 100 (fourth column), and 125 (fifth column) realizations for each of the Cartesian coordinate velocity vectors, with u shown in the top row, v shown in the middle row, and w shown in the bottom row. The color scale resolution is set to 1% of maximum range of the fluctuating values for each respective velocity component.

The same approach was used to ensure sufficient realizations were captured to ensure convergence of the second-order statistics and are shown in Figure 31 for the turbulence kinetic energy terms and Figure 32 for the Reynolds Shear Stress terms.

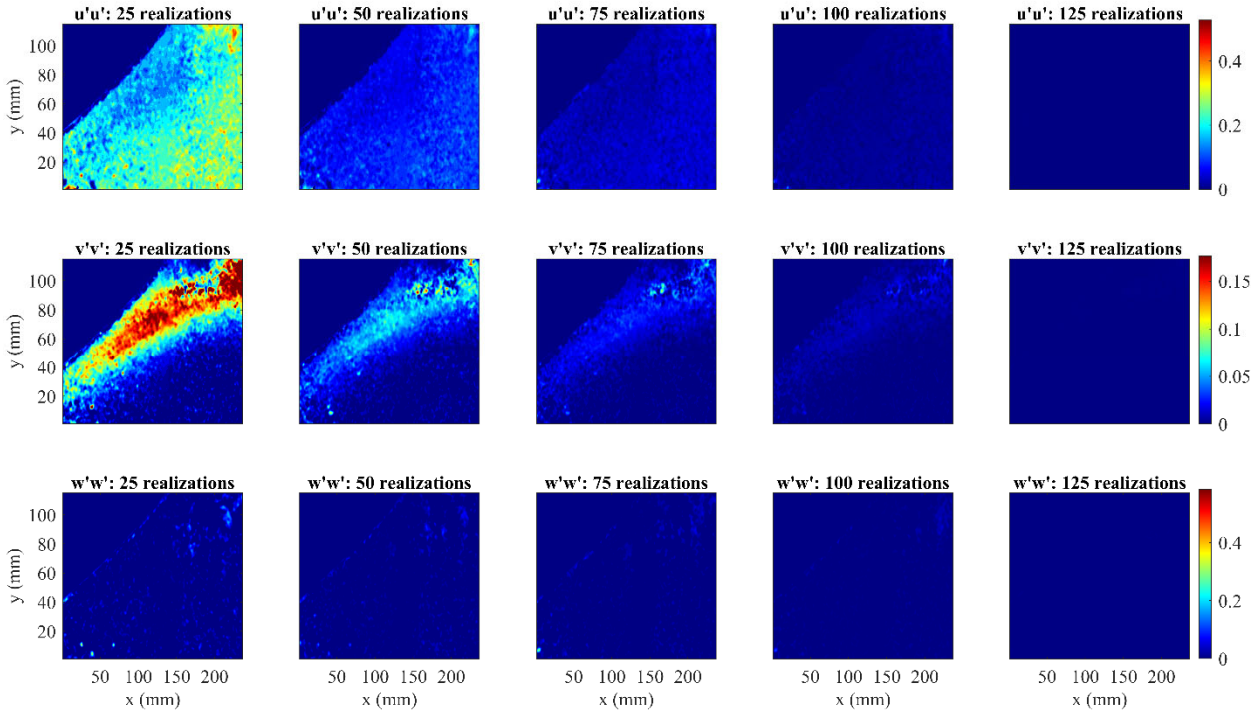

Figure 31: Convergence of Turbulence Kinetic Energy ($u_i u_i$) over successive realizations. These values were calculated by taking the cumulative average over the stated number of realizations and subtracting the mean, which includes 100 realizations. The range of the contour colors is 1% of the maximum range.

The blue fields in the last column mean that all turbulence intensity is within about 0.1 of 1% (0.01%) of the maximum range (e.g. abs(min($u'u'$) – max($u'u'$))).

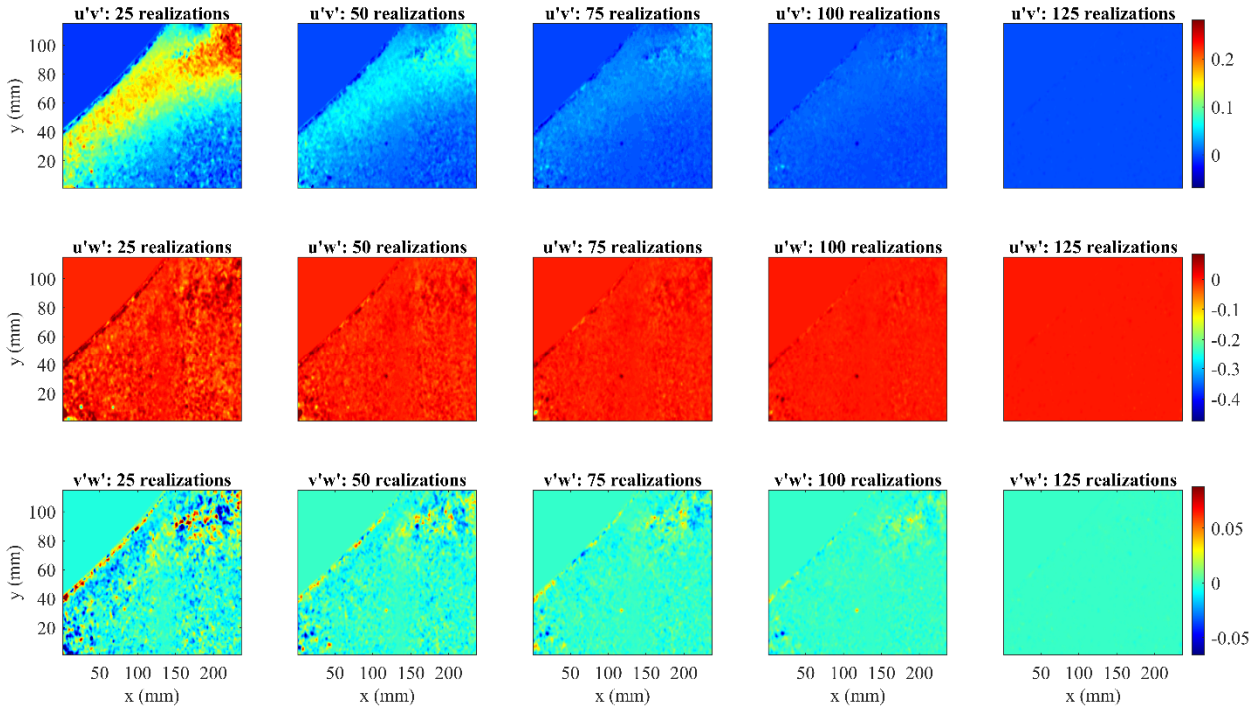

Figure 32: Convergence of the Reynolds Shear Stress ($u_i u_j$)

3.3. **Force and Moment Measurements**

Forces and moments in all three axes were measured simultaneously for angles of 2.5°, 5°, 10°, and 20° over a range of Reynolds numbers from just below 1×10^6 to just above 3×10^6, for both smooth and tripped models. In the following plots, found in Figure 33-35, the solid markers are for the tripped case and open are smooth. The force in the y-direction (i.e. the "lift") is shown in Figure 33.

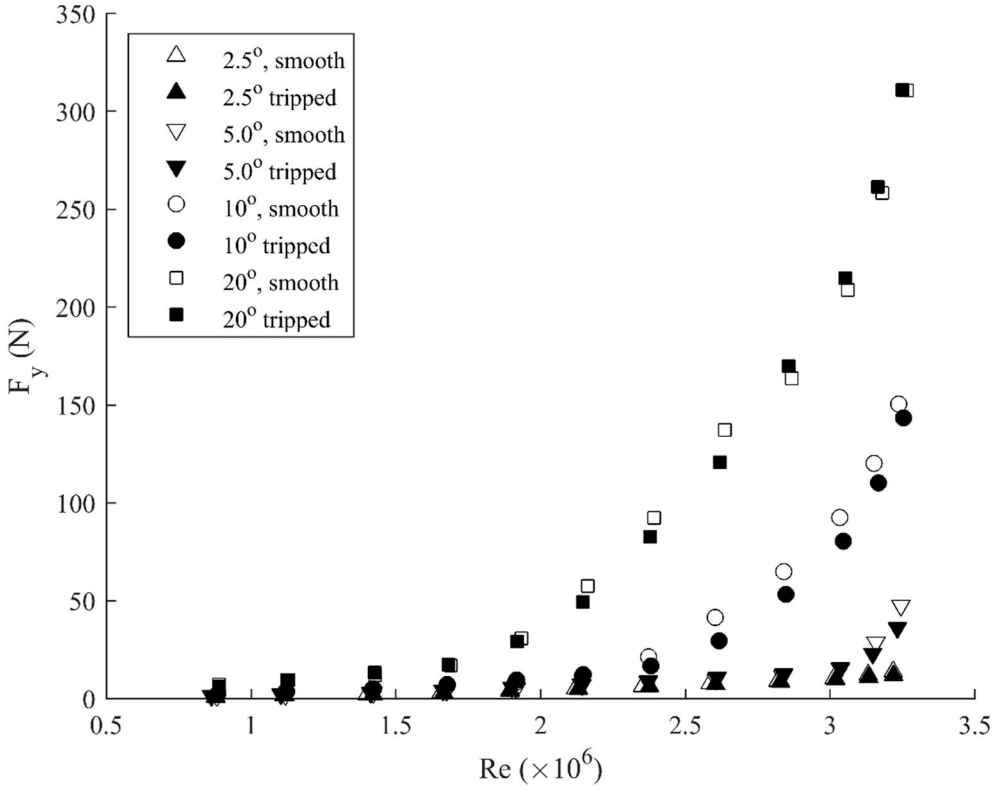

Figure 33: Dimensional Force in the y-direction (i.e. "lift"), as a function of Reynolds number for varying angles of attack (shown as different marker symbols) for the smooth and tripped body (shown as white and black markers, respectively)

For Reynolds numbers around 1×10^6, the forces for each angle of attack are of the same order of magnitude. As Reynolds number increases above 1.5×10^6 the force in the 20° case starts to diverge, followed by 2.0×10^6 in the 10° case and 3×10^6 in the 5° case. Previous experiments have shown that for increasing Reynolds number and angle of attack, the separated region moves upstream, widening the wake and increasing the net force on the body. These observations are consistent with the measurements of the present study. It also appears that the trip has little effect on the force.

The force coefficient is defined as:

$$C_{F,i} = \frac{F_i}{\frac{1}{2}\rho U^2 \pi R^2} \tag{13}$$

Where F_i is the force in one of the three Cartesian coordinate directions, ρ is the water density, U_∞ is the mean tunnel speed, and r is the semi-minor axis length (i.e. half the minor diameter). Results are shown in Figure 34.

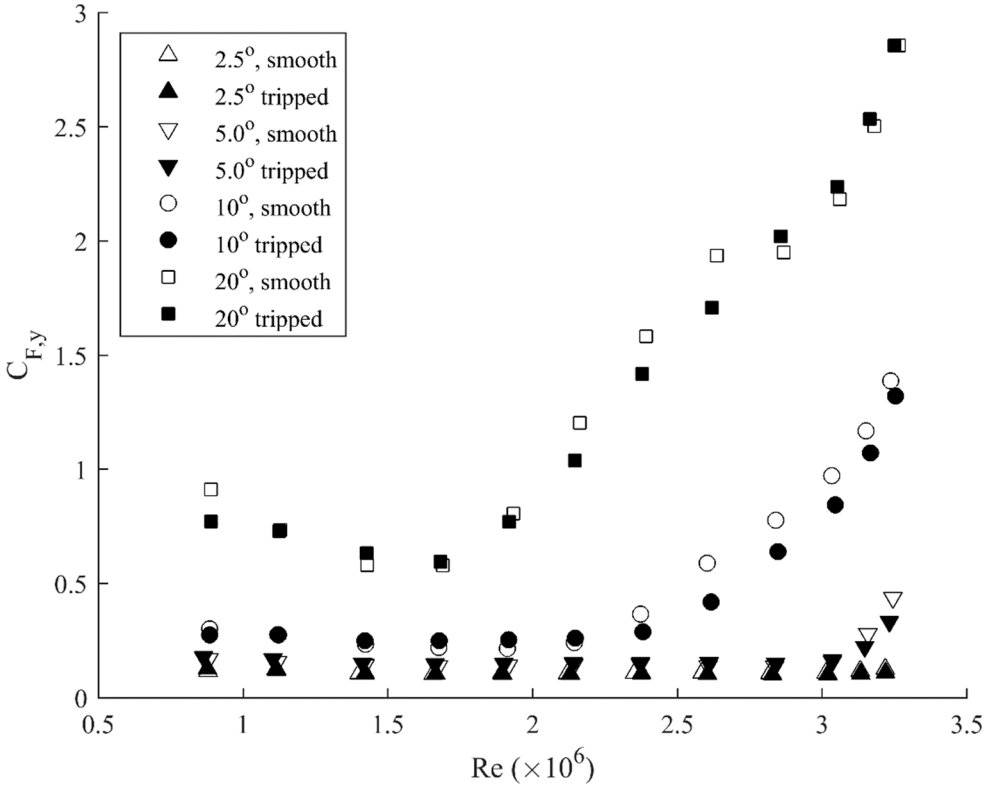

Figure 34: Force coefficient in the y-direction ("lift") as a function of length-based Reynolds number. White markers indicate data for the smooth body. Black markers indicate data for the tripped body. Each different marker shape indicates a particular angle of attack.

In all but the case with the lowest angle of attack, the coefficient of force decreases slightly from a Reynolds number of just under 1×10^6 to an inflection point: just above 3×10^6 for the 5° case, at approximately 2×10^6 for the 10° case, and at approximately 1.7×10^6 for the 20° case; decreasing for increasing angles of attack. For Reynolds numbers above this inflection point, the force coefficient increases rapidly, suggesting that the primary separation point is moving upstream on the body, widening the wake. The lateral fields of view, contained in Appendices I-P, support this conclusion, showing vortex formation at fields of view further upstream (i.e. lower x/L) with increasing Reynolds number and angle of attack. This is also observed in the longitudinal fields of view though it is more difficult to discern the bounds of the separated region in these figures. The agreement between the smooth and tripped data suggests that the trip is not having much influence, a conclusion supported by the mean velocity results.

Moments were also measured for each angle of attack and Reynolds number combination for both the smooth and tripped body. The dimensional results for the moment about the z-axis (horizontal) are presented in Figure 35.

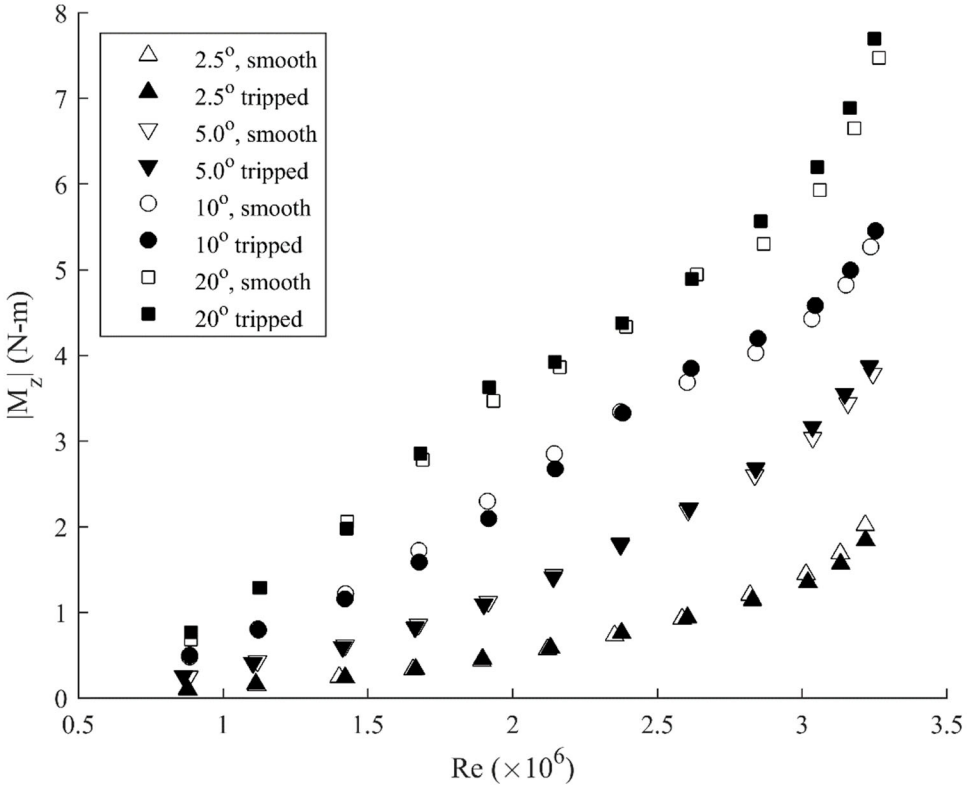

Figure 35: Moment in the z-direction (i.e. "pitch"), as a function of Reynolds number for varying angles of attack (shown as different marker symbols) for the smooth and tripped body (shown as white and black markers, respectively). These results are shown as a magnitude for readability. An increasing moment translates to a stronger moment tending to rotate the major axis of the body away from the direction of mean flow.

The pitching moment follows a gradual increase for each angle up to a Reynolds number of about 3×10^6 after which each appears to start increasing more rapidly. The pitching moment is a balance between the forces acting on the upstream half of the body versus the downstream half. An increasing moment means that the force on the upstream half is growing relative to that of the downstream half. This is consistent with the expansion of the separated region, causing increasing disparity between the pressure acting on the upstream (windward) side of the body as compared to the downstream (leeward) side of the body. Consistent with the force measurement observations, the trip does not appear to influence the flow compared to the smooth body case.

Similarly, the moment coefficient was calculated using the following expression:

$$C_{M,i} = \frac{M_i}{\frac{1}{2}\rho U^2 \pi R^3} \tag{14}$$

Where M is the moment, measured in one of the three Cartesian coordinate directions. The moment coefficient around the z-axis (i.e. the pitch moment), plotted as a magnitude for readability, is included in Figure 36.

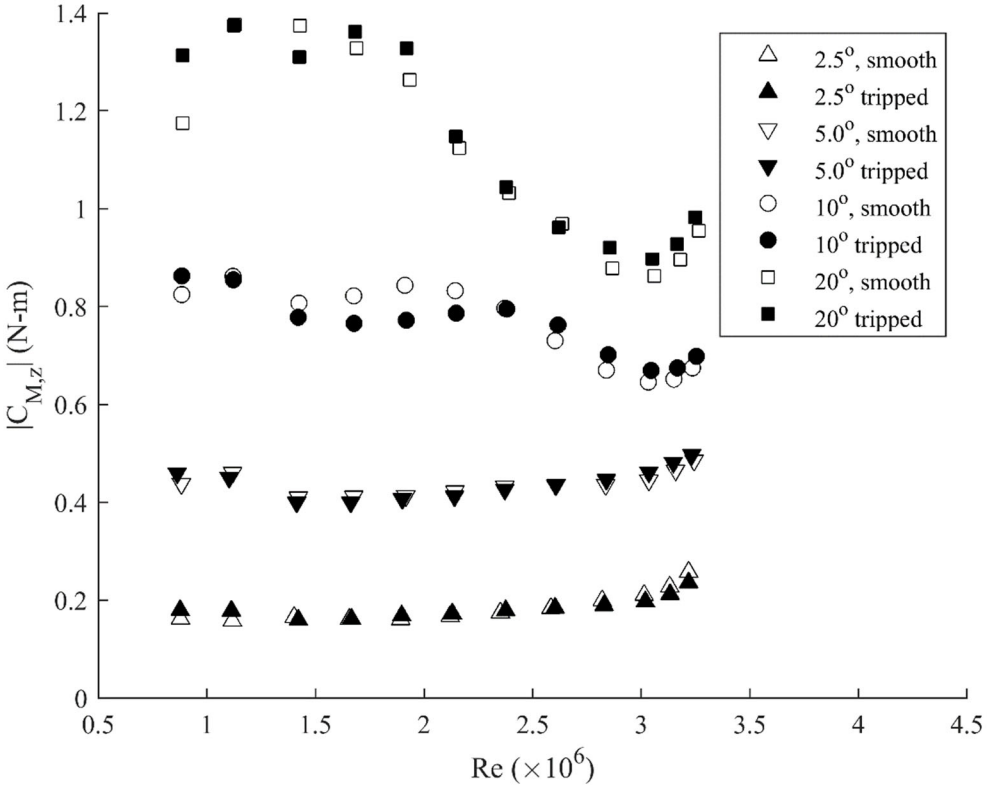

Figure 36: Moment coefficient in the *z*-direction (i.e. "pitch") as a function of length-based Reynolds number. White markers indicate data for the smooth body. Black markers indicate data for the tripped body. Each different marker shape indicates a particular angle of attack.

At the lowest angles of inclination, there is little discernable difference between the smooth and tripped bodies, and little variation with Reynolds number until a Reynolds number of 3×10^6 is reached, where a slight increase in the moment coefficient is noted. As angle of inclination is increased, the moment coefficient changes considerably over the Reynolds number range, increasing again as Reynolds number passes 3×10^6. These phenomena are primarily driven by the change in velocity, but the increase in moment coefficient at all angles near 3×10^6 appears to be driven by the inflection point shown in Figure 35.

4. Conclusions

A 6:1 prolate spheroid, measuring 0.432 m in length was tested in the large recirculating water tunnel at the U.S. Naval Academy. The mean velocity was changed such that the length-based Reynolds number was varied from 1 to 3×10^6, the angle of inclination was varied from 2.5° to 20°, and one boundary layer trip geometry was evaluated.

As Reynolds number increases, wake topology remains relatively constant while the vertical velocity and vorticity increase. Comparing the vertical velocity flow field in the 20° case at Reynolds numbers of 1×10^6 to 3×10^6, the relative magnitude of the vertical velocity increases roughly 10%. Also, in the 20° case, vorticity increases in magnitude as Reynolds number increases and as position downstream from the nose of the spheroid increases. Based on the findings of Ahn and Simpson, it is expected that this research operates in a range of Reynolds number dependence, and the variation in both vertical velocity and vorticity as Reynolds number changes support this [3].

As angle of inclination increases, separation moves upstream, resulting in a more developed wake in the downstream region. Larger angles of inclination result in a larger magnitude in the vertical velocity, out of plane velocity, vorticity, and turbulence, when compared to lower angles of inclination at the same relative position along the body of the spheroid. More specifically, in the vertical velocity flow field, when Reynolds number was held constant, the relative magnitude of the vertical velocity in the wake of the spheroid at 2.5° was less than 25% of that in the wake of the spheroid at 20° in both the 1 and 3×10^6 Reynolds number cases. The observed trends, movement of separation upstream and increased three-dimensionality in the flow as angle of inclination increases, agree with the findings of both Fu et al. [4] and Goody, Simpson, and Engel [5].

Comparing the tripped and smooth configurations, there was little difference between the two flow fields. Slight differences were observed in the vertical velocity at 2.5°, but further examination is required in order to quantify the difference between the two cases at 2.5°. Differences between the tripped and smooth configurations were also observed in the vorticity and turbulence at 20°. In the tripped case, the vorticity and turbulence were more similar across all Reynolds numbers than in the smooth case, indicating that the trip was in fact effective in regards to vorticity and turbulence at 20°. The effect of trip on vorticity, as show in Figure 27, shows strong agreement with a previous study conducted by Fu et al. in which it was determined that the trip results in a larger area of vortical flow in the 2.1×10^6 Reynolds number case [4]. Due to the inconsistencies observed when examining the trip, its effectiveness is inconclusive at this time, and the use of alternative tripping methods and geometries should be examined in follow on studies.

Looking at both the force and moment data, the raw data and the non-dimensionalized data, there is not an observable difference between the tripped and smooth configurations. Both the force and moment coefficients show an inflection point at approximately 3×10^6 Reynolds number. This suggests separation moving upstream with increasing Reynolds number and angle of attack, which is supported by previous observations.

5. References

[1] H. U. Meier and H. P. Kreplin, "Experimental Investigation of the Transition and Separation Phenomena on a Body of Revolution," in *International Symposium on Turbulent Shear Flow*, London, 1979.

[2] K. M. Barber and R. Simpson, "Mean Velocity and Turbulence Measurements of Flow Around a 6:1 Prolate Spheroid," *Office of Naval Research Applied Hydrodynamics Research Program,* 1990.

[3] S. Ahn and R. Simpson, "Cross-flow separation on a prolate spheroid at angles of attack," *In 30th Aerospace Sciences Meeting and Exhibit,* p. 428, 1992.

[4] T. C. Fu, A. Shekarriz, J. Katz and T. T. Huang, "The flow structure in the lee of an inclined 6:1 prolate spheroid," *Journal of Fluid Mechanics 269,* pp. 79-106, 1994.

[5] M. Goody, R. Simpson and M. Engel, "Mean velocity and pressure and velocity spectral measurements within a separated flow around a prolate spheroid at incidence," *In 36th AIAA Aerospace Sciences Meeting and Exhibit,* p. 630, 1998.

[6] C. J. Chesnakas and R. L. Simpson, "Detailed investigation of the three-dimensional separation about a 6-1 prolate spheroid," *AIAA Journal 35,* pp. 990-999, 1997.

[7] B. Johnson and J. Zseleczky, "The History of the Naval Academy Hydromechanics Laboratory," in *Proceedings of the 29th American Towing Tank Conference*, Annapolis, MD, 2010.

[8] G. West and C. Apelt, "The Effects of Tunnel Blockage and Aspect Ratio on the Mean Flow Past a Circular Cylinder with Reynolds Numbers Between 10,000 and 100,000.," *Journal of Fluid Mechanics,* vol. 114, pp. 361-377, 1981.

[9] J. P. Peck and E. E. Lust, "Characterization of the Far Wake of an Inclined 6:1 Prolate Spheroid," U.S. Naval Academy, Annapolis, 2020.

[10] C. Shih, "Turbulent Wake Flow Behind a Circular Cylinder," 28 August 2002. [Online]. Available: http://www.eng.fsu.edu/~shih/succeed/cylinder/cylinder.htm. [Accessed 25 October 2019].

[11] K. Kiger, "PIV Basics: Correlation," July 2015. [Online]. Available: http://www.civil.ist.utl.pt/~ruif/SUMMER_SCHOOL/presentations/PIV_basics_correlation_final.pdf. [Accessed 06 May 2020].

[12] B. R. Elbing, L. Daniel, Y. Farsiani and C. E. Petrin, "Design and Validation of a Recirculating, High-Reynolds Number Water Tunnel," *Journal of Fluids Engineering,* vol. 140, no. August 2018, pp. 081102-1-6, 2018.

[13] S. Ahn and R. Simpson, "Cross-Flow Separation on a Prolate Spheroid at Angles of Attack," in *AIAA, 30th Aerospace Sciences Meeting and Exhibit*, Reno, 1992.

[14] B. Munson, T. Okiishi, W. Huebsch and A. Rothmayer, Fundamentals of Fluid Mechanics, 7th Ed., Hoboken: John Wiley & Sons, 2013.

[15] E. Lust, K. Flack and L. Luznik, "Survey of the Near Wake of an Axial-Flow Hydrokinetic Turbine in Quiescent Conditions," *Renewable Energy ,* vol. 129, pp. 92-101, 2018.

[16] S. Pope, Turbulent Flows, Cambridge: Cambridge University Press, 2000.

[17] S. Ahn, "An experimental study of flow over a 6:1 prolate spheroid at incidence," Ph.D. dissertation, Virginia Polytechnic Institute and State University, Blacksburg, 1992.

Appendix A: 2.5°, Reynolds number of 1×10^6, 2×10^6, and 3×10^6 (top to bottom), Longitudinal, and Smooth

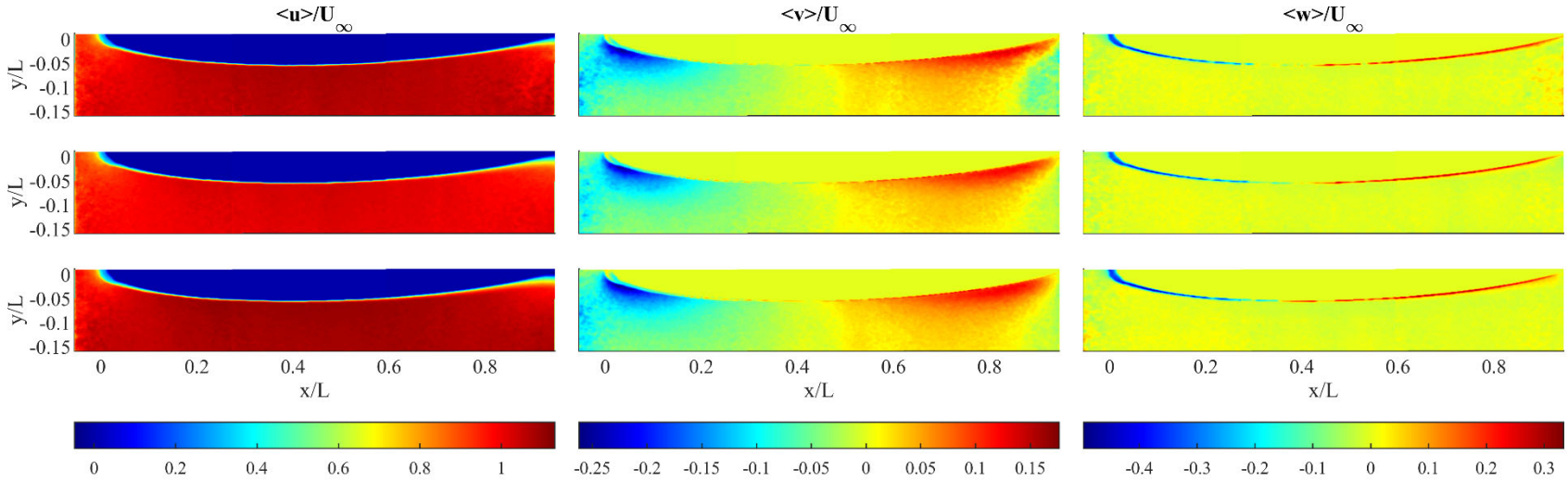

Appendix B: 2.5°, Reynolds number of 1×10^6, 2×10^6, and 3×10^6 (top to bottom), Longitudinal, Tripped

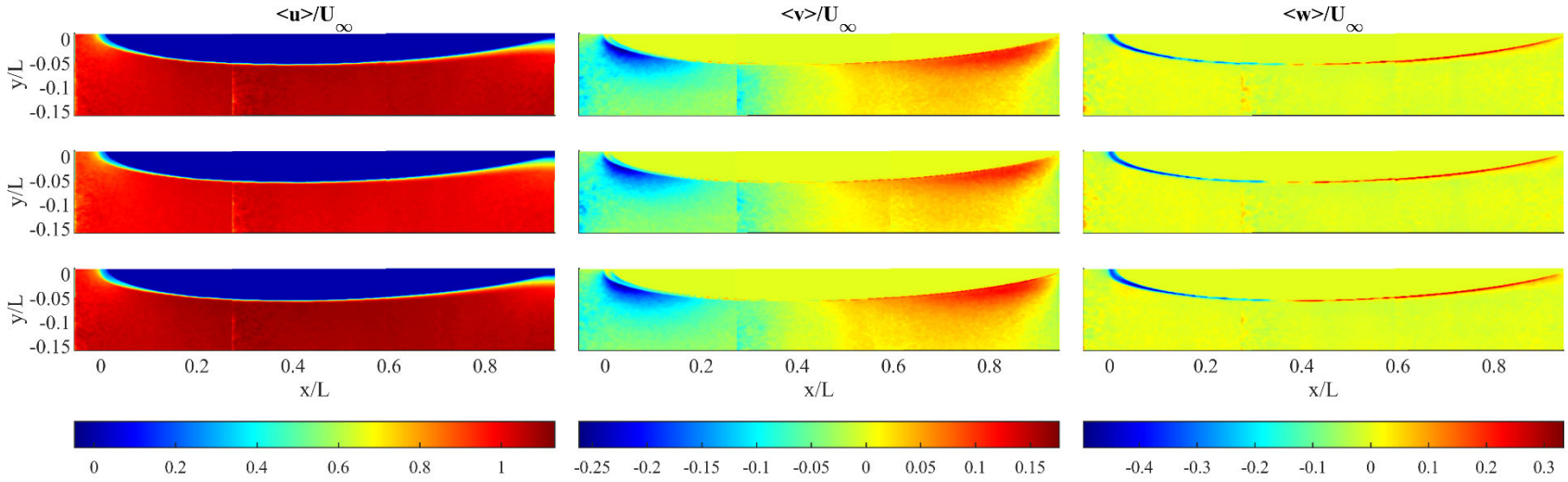

Appendix C: 5°, Reynolds number of 1×10^6, 2×10^6, and 3×10^6 (top to bottom), Longitudinal, Smooth

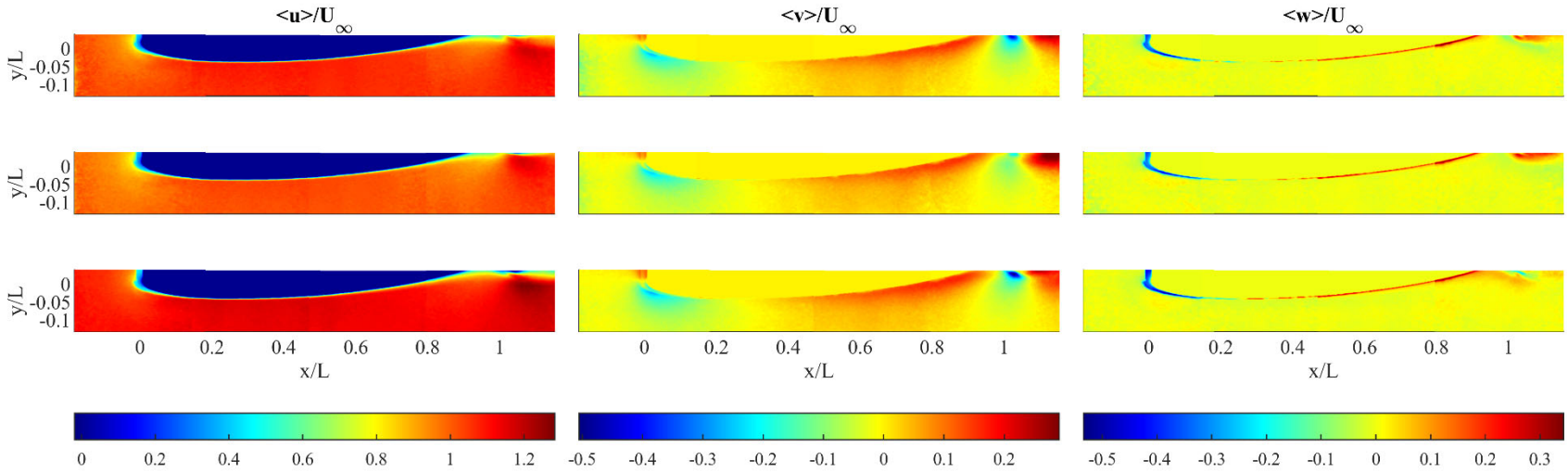

Appendix D: 5°, Reynolds number of 1×10^6, 2×10^6, and 3×10^6 (top to bottom), Longitudinal, Tripped

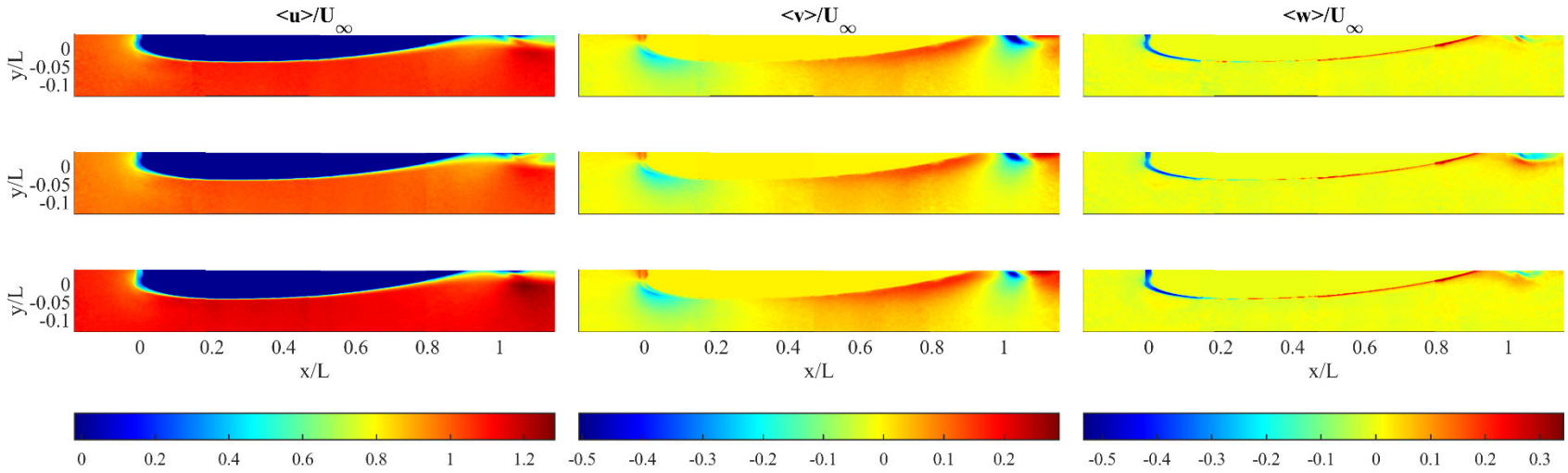

Appendix E: 10°, Reynolds number of 1×10^6, 2×10^6, and 3×10^6 (top to bottom), Longitudinal, Smooth

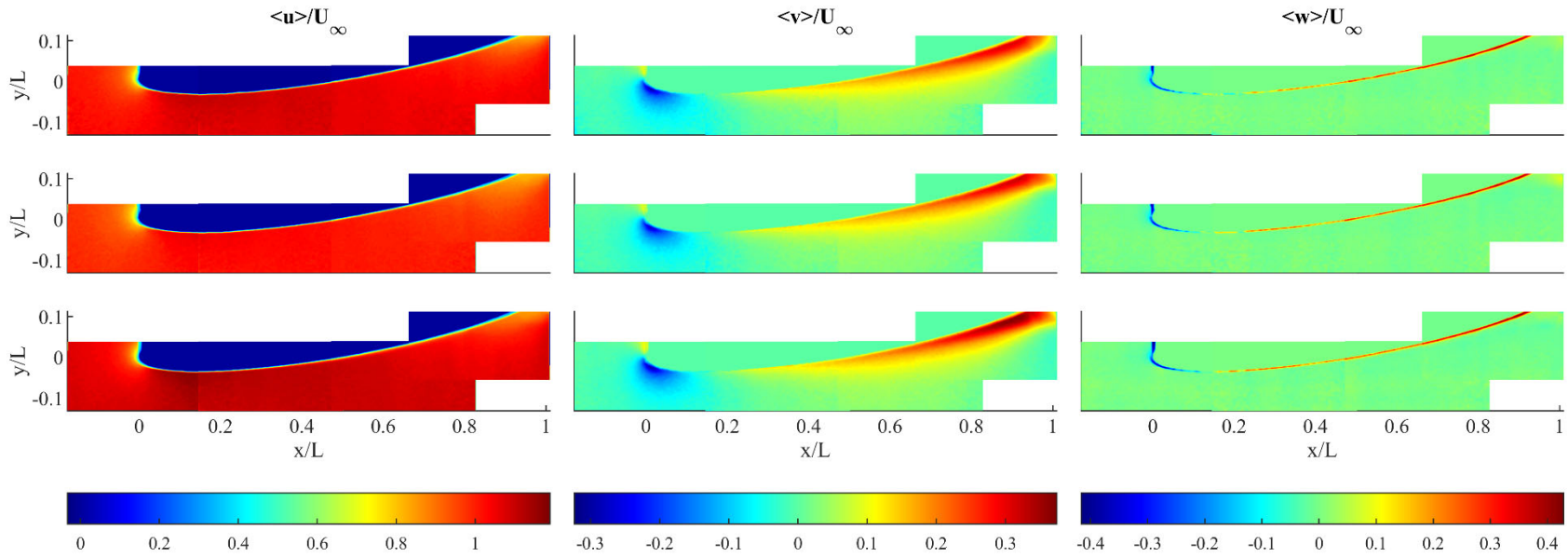

Appendix F: 10°, Reynolds number of 1×10^6, 2×10^6, and 3×10^6 (top to bottom), Longitudinal, Tripped

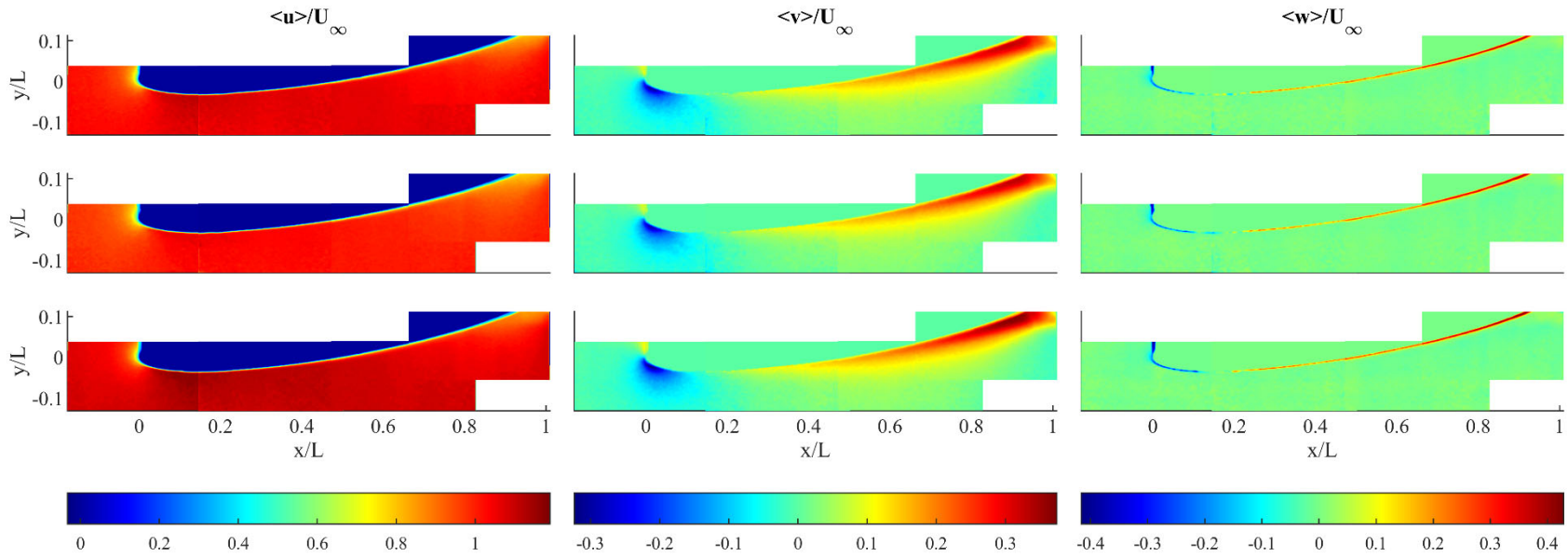

Appendix G: 20°, Reynolds number of 1×10^6, 2×10^6, and 3×10^6 (top to bottom), Longitudinal, Smooth

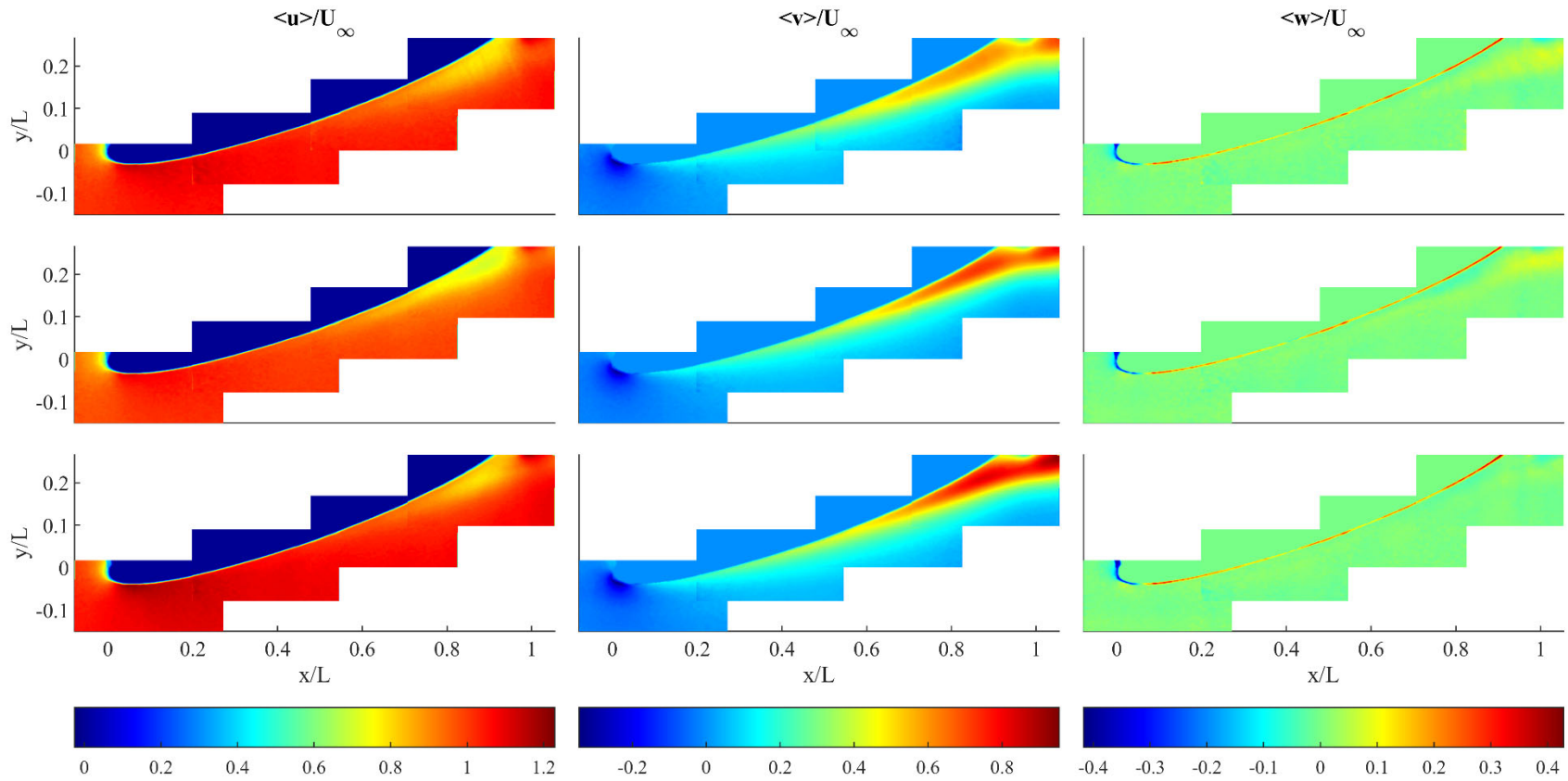

Appendix H: 20°, Reynolds number of 1×10^6, 2×10^6, and 3×10^6 (top to bottom), Longitudinal, Tripped

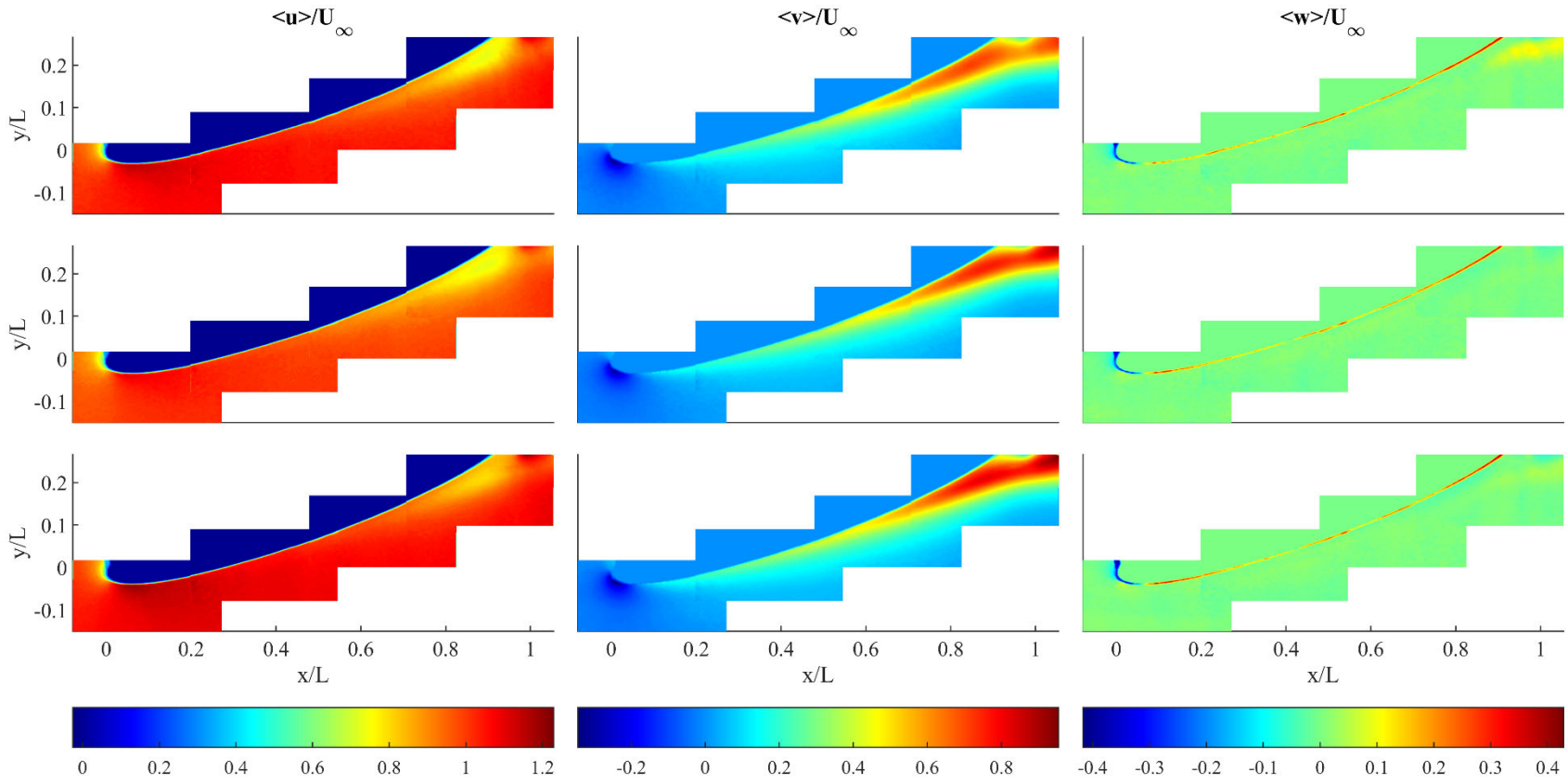

Appendix I: 2.5°, Reynolds number of 1×10^6, 2×10^6, and 3×10^6 (top to bottom), Velocities ***u***, ***v***, and ***w*** (top to bottom), Lateral, Smooth

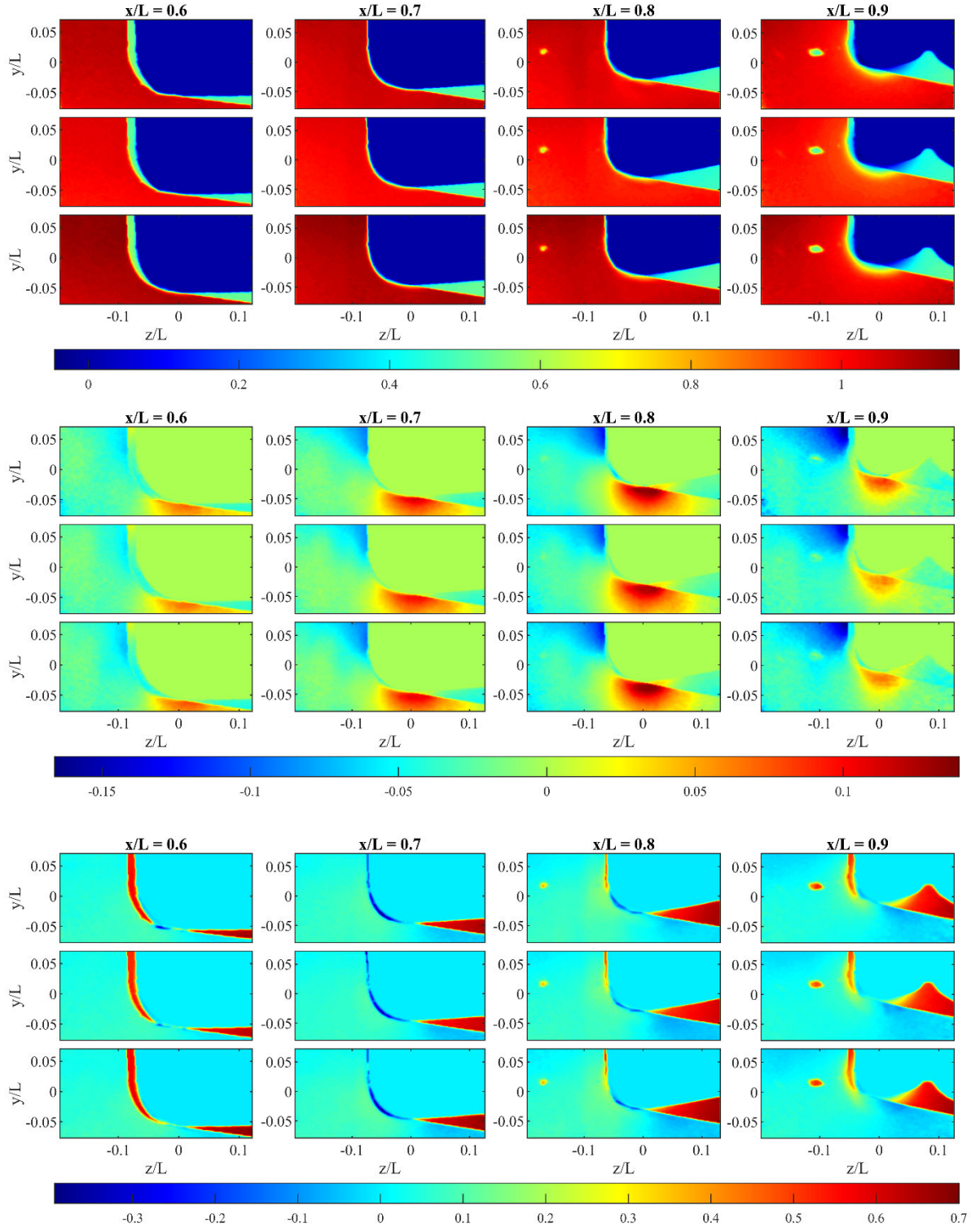

Appendix J: 2.5°, Reynolds number of 1×10^6, 2×10^6, and 3×10^6 (top to bottom), Velocities ***u***, ***v***, and ***w*** (top to bottom), Lateral, Tripped

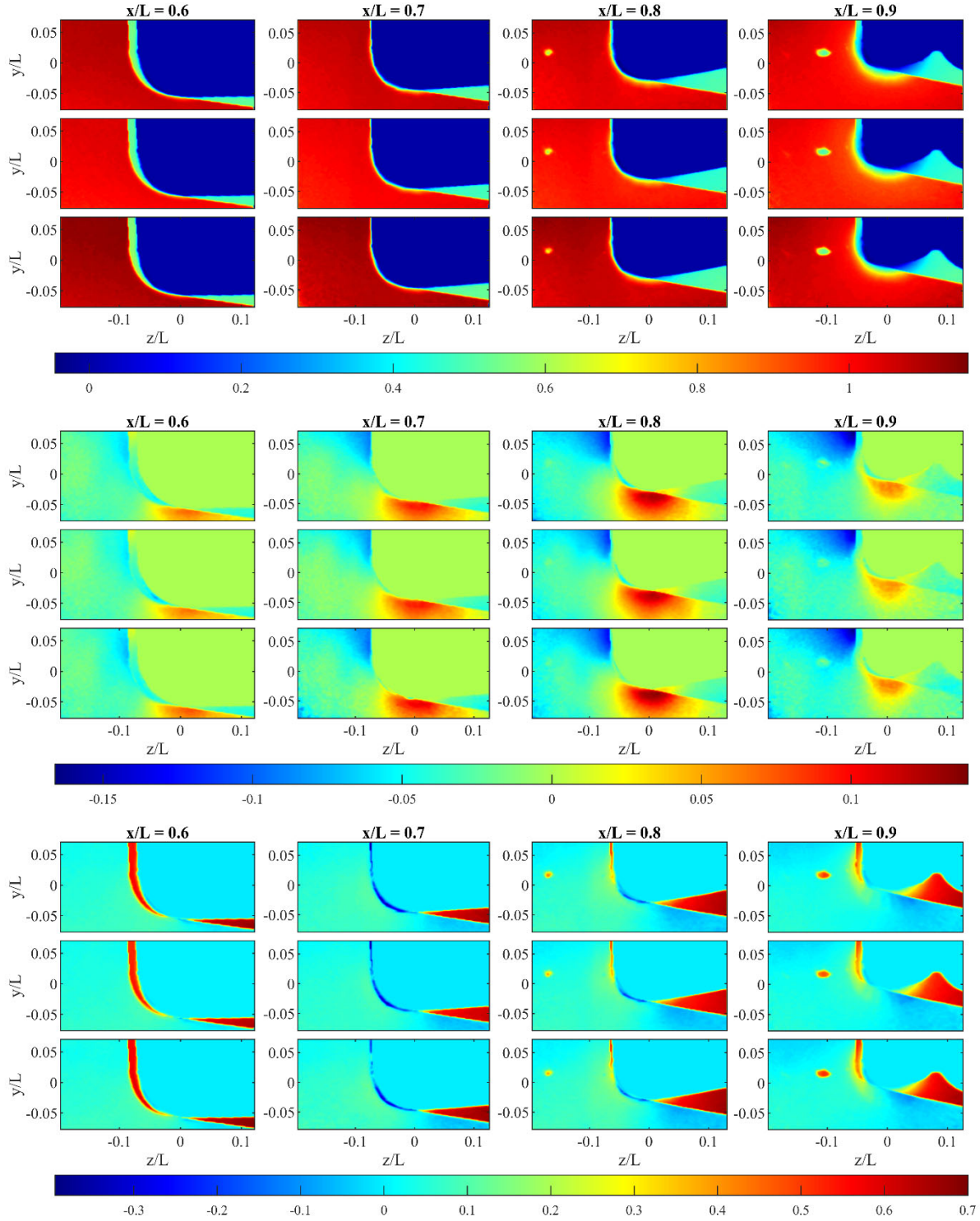

Appendix K: 5°, Reynolds number of 1×10^6, 2×10^6, and 3×10^6 (top to bottom), Velocities ***u***, ***v***, and ***w*** (top to bottom), Lateral, Smooth

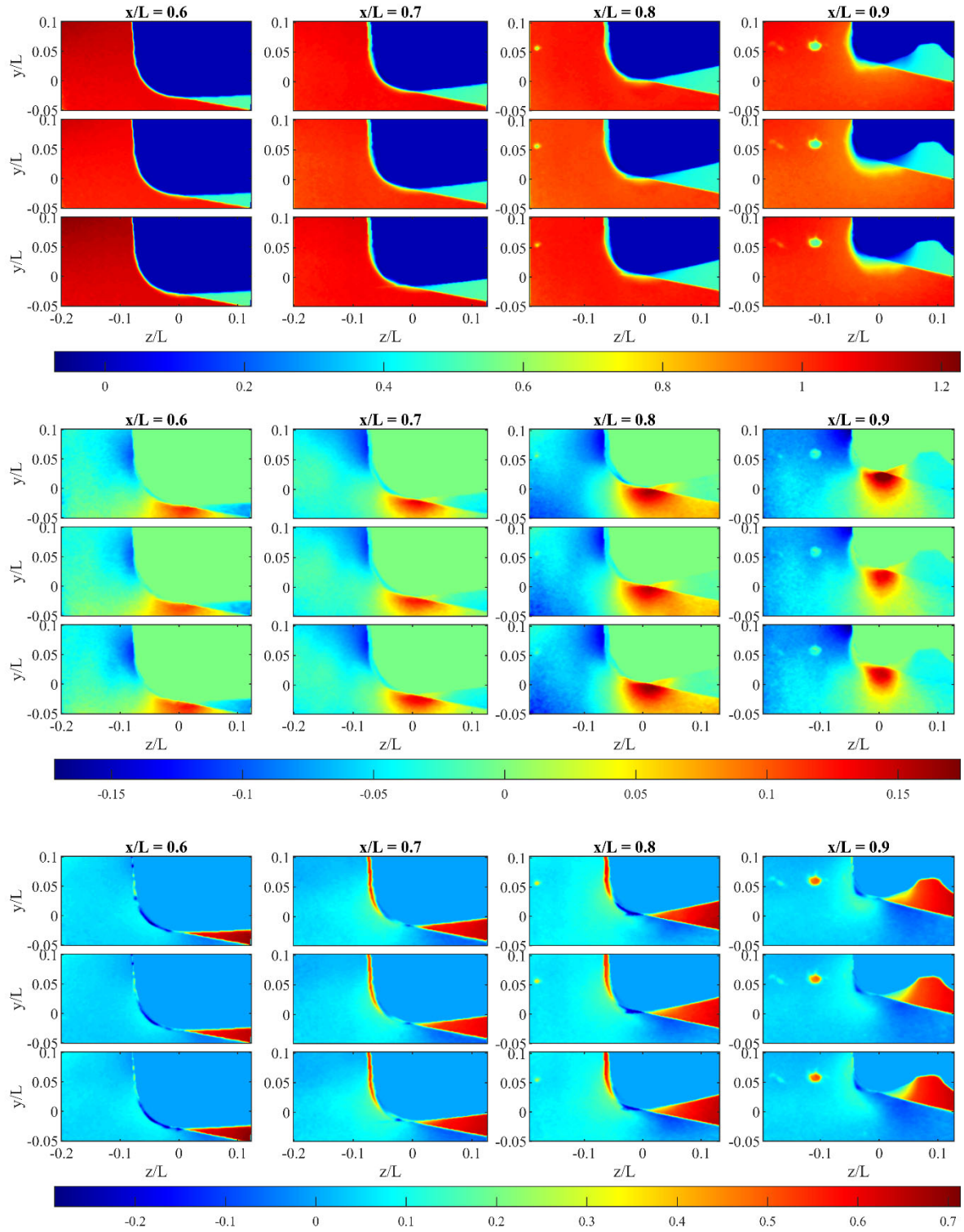

Appendix L: 5°, Reynolds number of 1×10^6, 2×10^6, and 3×10^6 (top to bottom), Velocities ***u***, ***v***, and ***w*** (top to bottom), Lateral, Tripped

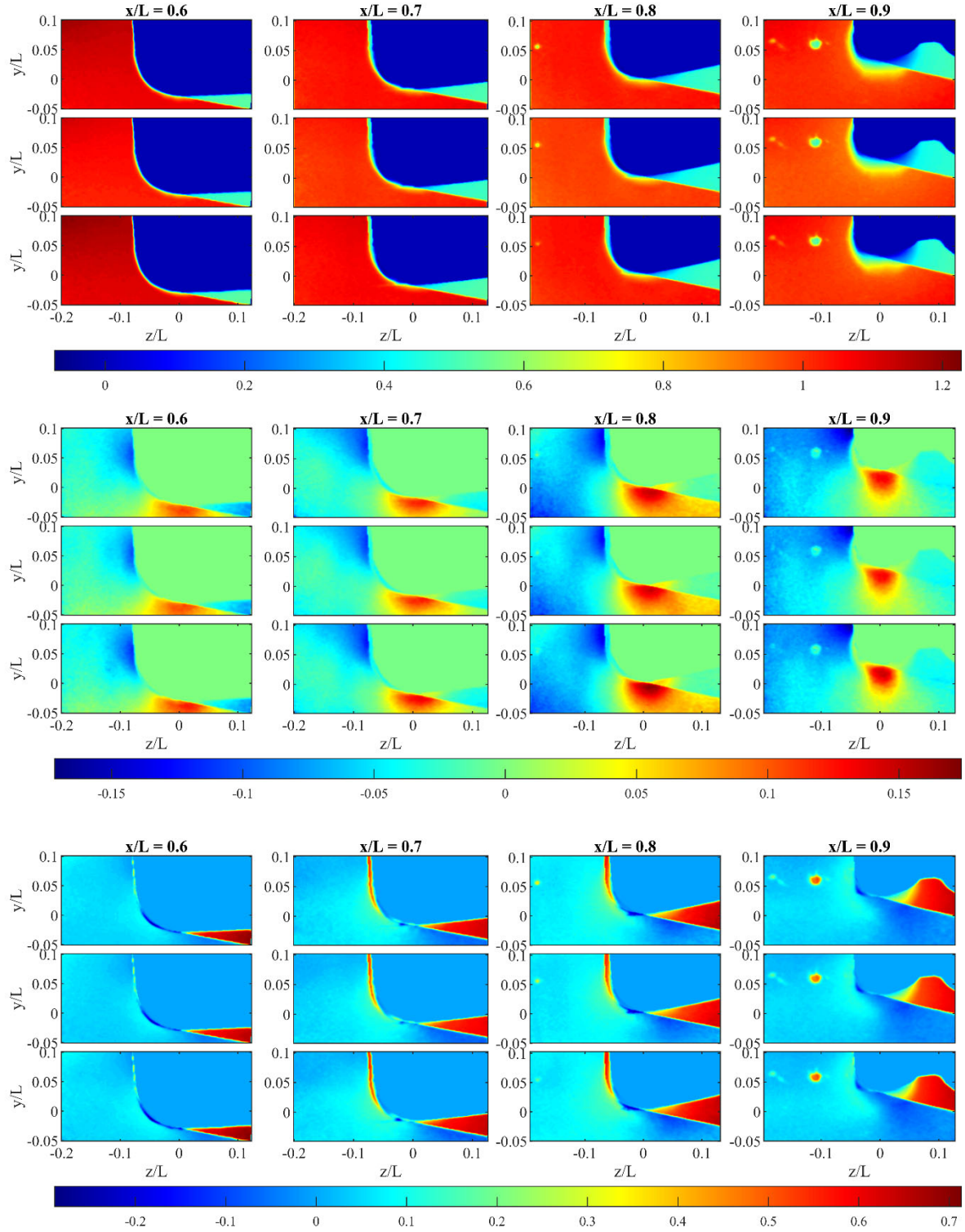

Appendix M: 10°, Reynolds number of 1×10^6, 2×10^6, and 3×10^6 (top to bottom), Velocities ***u***, ***v***, and ***w*** (top to bottom), Lateral, Smooth

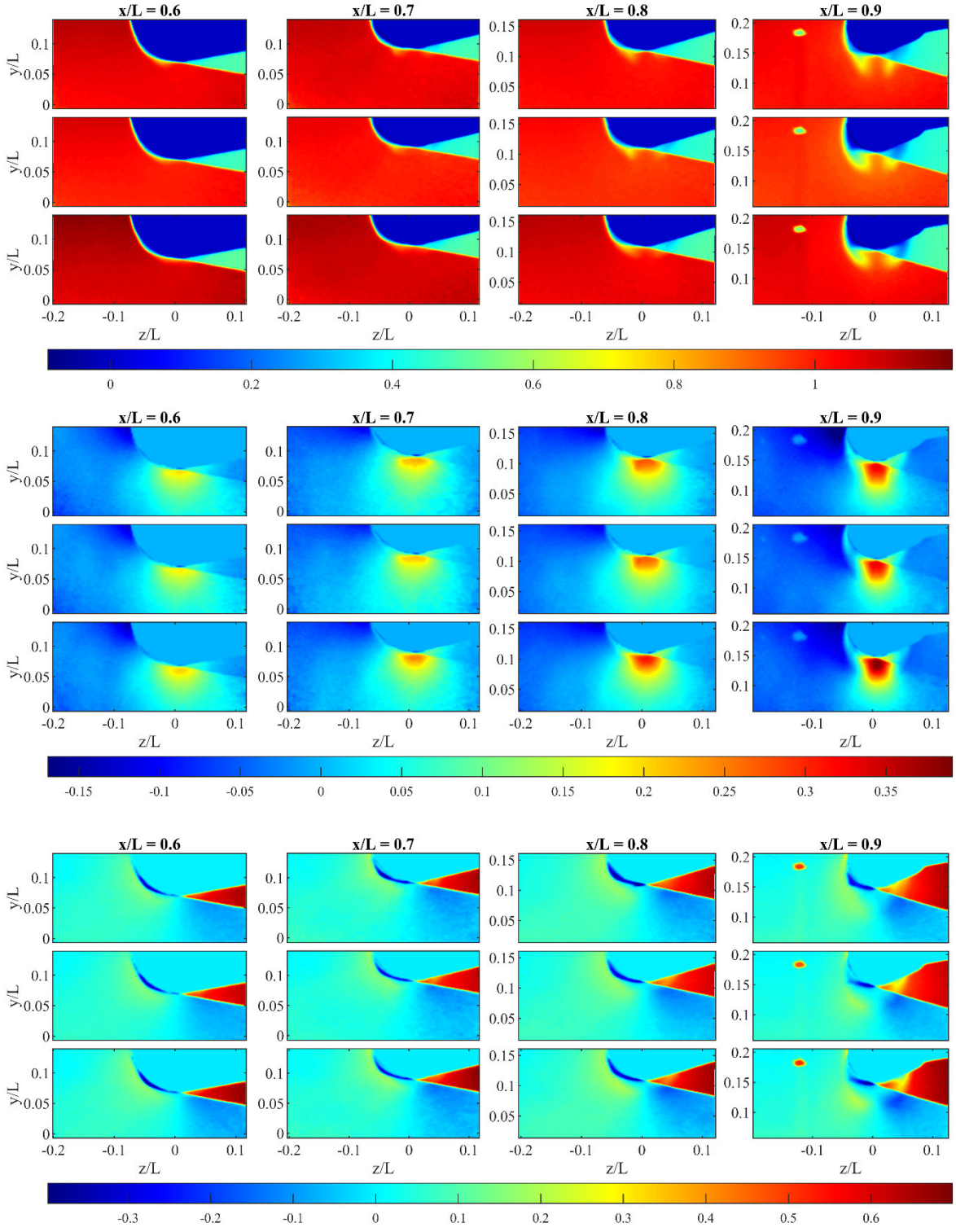

Appendix N: 10°, Reynolds number of 1×10^6, 2×10^6, and 3×10^6 (top to bottom), Velocities ***u***, ***v***, and ***w*** (top to bottom), Lateral, Tripped

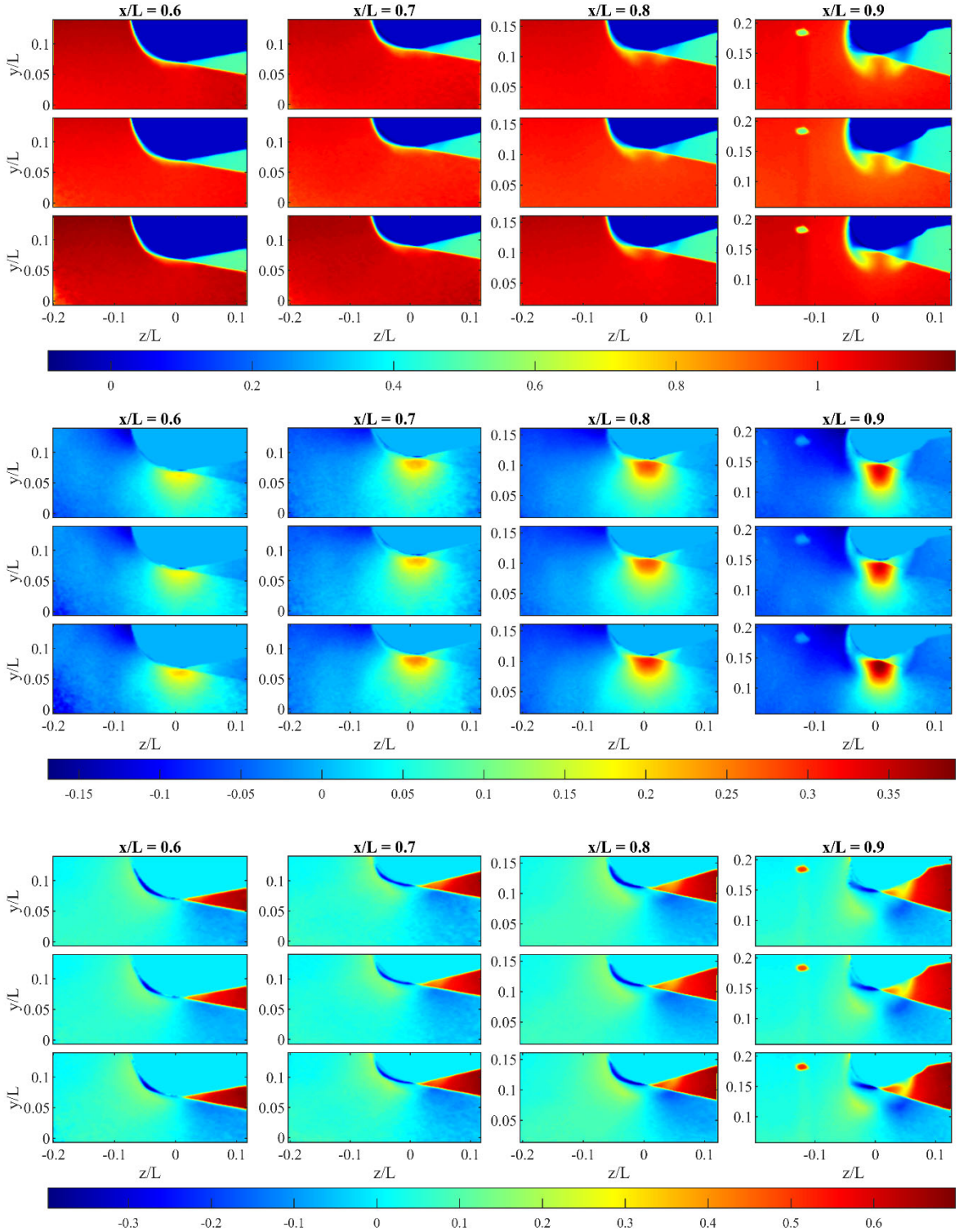

Appendix O: 20°, Reynolds number of 1×10^6, 2×10^6, and 3×10^6 (top to bottom), Velocities ***u***, ***v***, and ***w*** (top to bottom), Lateral, Smooth

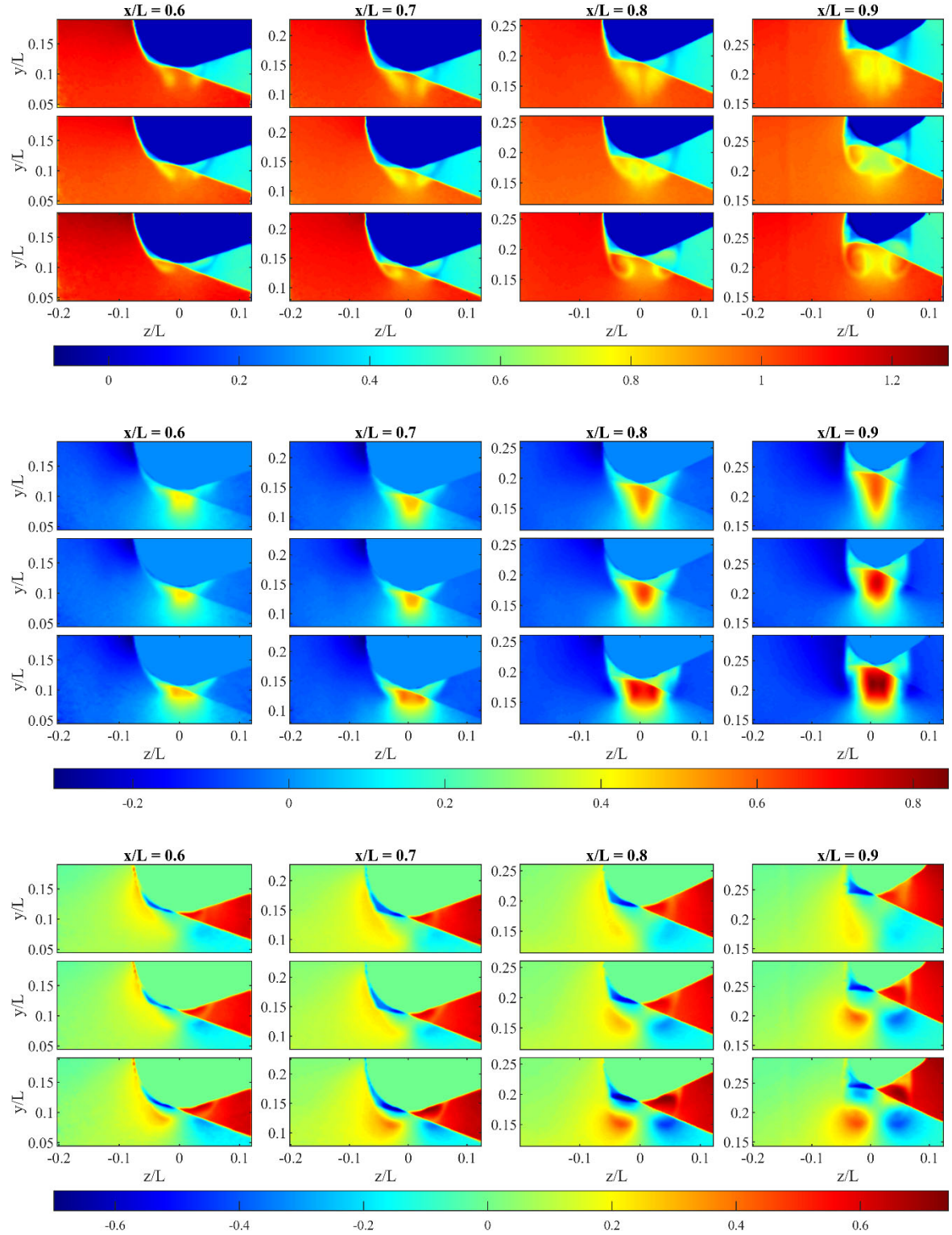

Appendix P: 20°, Reynolds number of 1×10^6, 2×10^6, and 3×10^6 (top to bottom), Velocities ***u***, ***v***, and ***w*** (top to bottom), Lateral, Tripped